AMERICAN METEOROLOGICAL SOCIETY

Journal of Atmospheric and Oceanic Technology

The DOI for this manuscript is doi: 10.1175/2010JTECHA1356.1

Attenuation Correction and Hydrometeor Classification of High-Resolution, X-band, Dual-Polarized Mobile Radar Measurements in Severe Convective Storms

Jeffrey C. Snyder[1], Howard B. Bluestein[1], Guifu Zhang[1], Stephen J. Frasier[2]

[1]School of Meteorology

University of Oklahoma

Norman, OK 73072

[2]Microwave Remote Sensing Laboratory

University of Massachusetts – Amherst

Amherst, MA 01003

Submitted to J. Atmos. Ocean. Technology

Originally Submitted: 26 June 2009

Revised: 10 November 2009, 27 February 2010

Corresponding author address:

Jeffrey Snyder

School of Meteorology, University of Oklahoma,

120 David L Boren Blvd., Suite 5900, Norman, OK, 73072

Email: wxguy1@ou.edu

Abstract

X-band and shorter radar wavelengths are preferable for mobile radar systems because a narrow beam can be realized with a moderate sized antenna. However, attenuation by precipitation becomes progressively more severe with decreasing radar wavelength. As a result, X-band has become a popular choice for meteorological radar systems that balances these two considerations. Dual-polarization provides several methods by which this attenuation (and differential attenuation) can be detected and corrected, mitigating one of the primary disadvantages of X-band radars.

The dynamics of severe convective storms depend, to some extent, on the distribution and type of hydrometeors within the storm. In order to estimate the three-dimensional distribution of hydrometeors using X-band radar data, it is necessary to correct for attenuation before applying commonly used hydrometeor classification algorithms. Since 2002, a mobile, dual-polarized Doppler weather radar designed at the University of Massachusetts – Amherst has been used to collect high-resolution data in severe convective storms in the Plains. This study tests several attenuation correction procedures using dual-polarization measurements, along with a dual-frequency method using S-band WSR-88D and KOUN data. After correcting for attenuation and differential attenuation, a fuzzy logic hydrometeor classification algorithm, modified for X-band with KOUN data as a reference, is used to attempt a retrieval of hydrometeor types in observed severe convective storms.

1. Introduction

Doppler weather radar is one of the few remote-sensing platforms that can provide high spatial and temporal resolution measurements of severe convection. In fact, mobile Doppler weather radars have been used for more than a decade to observe convective storms, including those transmitting at W-band (Bluestein and Pazmany 2000), X-band (e.g., Wurman et al. 1997; Iwanami et al. 2001; Kramar et al. 2005), and C-band (Biggerstaff et al. 2005). Unfortunately, scattering simulations indicate that attenuation through rain at X-band is at least an order of magnitude larger than that at S-band and often several times larger than at C-band. Accurate quantitative and qualitative interpretation of X-band radar data can be significantly diminished if the effects of attenuation are not considered and corrected.

It is apparent that the rear-flank downdraft (RFD) in supercells plays a very important role in supercell tornadogenesis, even though the specific origins and dynamics of the RFD are not completely understood (Brandes 1978; Lemon and Doswell 1979; Wicker and Wilhelmson 1995; Dowell and Bluestein 1997). The type and size distribution of hydrometeors near and within the RFD and their associated impacts on the rates of evaporation, sublimation, precipitation loading, etc., may significantly affect the RFD and, consequently, tornadogenesis. Furthermore, as numerical modeling advances towards more sophisticated microphysics schemes and higher spatial and temporal resolutions, there arises a need for high-resolution observations to provide verification of hydrometeor type and distribution provided by the simulations. The practical impacts of hydrometeor type on supercell thermodynamic and kinematic fields are not the focus of this study; this paper presents the results of attenuation correction and hydrometeor classification within severe convection using high-resolution, X-band polarimetric data from a mobile radar as an exercise necessary before one can determine what hydrometeor types reveal

about storm dynamics and kinematics.

The polarimetric weather radar that serves as the main source of data for this paper – the University of Massachusetts X-Pol (hereafter referred to the "UMass X-Pol") – measures the following: radial velocity (V_R); radar reflectivity factor at horizontal ($Z_H^{'}$) and vertical polarization ($Z_V^{'}$), from which differential reflectivity ($Z_{DR}^{'}$,) can be calculated; co-polar cross-correlation coefficient at lag zero (ρ_{HV}); and total differential phase (Φ_{DP}). The last of these quantities is the sum of two components – backscatter differential phase (δ) and propagation differential phase (ϕ_{DP}):

$$\Phi_{DP} = \arg\left(\left\langle n f_{vv}^{(b)} f_{hh}^{(b)*} \right\rangle\right) + 2\int_0^r K_{DP}(r')dr' = \delta + \phi_{DP} \qquad (1)$$

where n is a proxy for the drop-size distribution (DSD), $f_{vv}^{(b)}$ and $f_{hh}^{(b)}$ are the amplitudes of the copolar terms of the backscattering matrix, and K_{DP} is the specific propagation differential phase. Since raindrops are oblate spheroids (for which the major axis nearly always is in the horizontal) and since most linearly-polarized polarimetric weather radars transmit in the horizontal and vertical, $K_{DP} > 0$ deg km^{-1} in rain. Hailstones, as well as ice crystals in a strong electric field, may be oriented such that the major axis of most particles is in the vertical, resulting in negative K_{DP}. Similarly, resonance effects associated with non-Rayleigh scattering in hail can result in $K_{DP} < 0$ deg km^{-1}. In addition, depending upon the method by which Φ_{DP} is processed and K_{DP} is calculated, gradients in δ with range may result in incorrect K_{DP} estimates; $K_{DP} < 0$ deg km^{-1} may be calculated in liquid precipitation as a result of gradients in δ with range.

Most of the previous work involving hydrometeor signatures in polarimetric radar data has pertained to S-band (e.g. Vivekanandan et al. 1999; Liu and Chandrasekar 2000; Straka et al. 2000; Schuur et al. 2003), and some important differences between S-band and X-band data are

noted where relevant. More details on polarimetric characteristics of different hydrometeor species observed at S-band are presented in Straka et al. (2000). As one example of a difference between S-band and X-band data, the presence of more pronounced resonance scattering at C-band and X-band compared to that at S-band may yield higher-than-expected Z_{DR} in hail and may prohibit the use of Z_{DR} for hail determination purposes, as noted by Ryzhkov et al. (2007a) and Kumjian and Ryzhkov (2008) for C-band data.

Though substantial overlap between hydrometeor types and various polarimetric variables remains, the availability of an expanded number of parameters provided by dual-polarized radar systems makes hydrometeor classification a more feasible feat. Unfortunately, without the ability to observe hydrometeor type at spatial and temporal resolutions near those of the UMass X-Pol, it is currently impossible to verify fully the results of hydrometeor classification. Three cases are examined in this manuscript – one of total attenuation within a tornadic supercell (29 May 2004), one of very minor attenuation within a tornadic supercell (12 May 2004), and one of total attenuation within a squall line (21 May 2007).

The attenuation correction techniques used in this study are outlined in section 2, which also contains a brief discussion of the hydrometeor classification scheme and the radar platform used in this study. The results of attenuation correction and hydrometeor classification, in addition to discussion of notable polarimetric signatures, for the three cases are given in section 3. A review of the results and a discussion of the implications, problems, and future work conclude this paper.

2. Methodology

a. Attenuation correction

Measured and intrinsic (or unattenuated) $Z_{H,V}$, in units of dBZ, are related by

$$Z'_{H,V}(r) = Z_{H,V}(r) - 2\int_0^r A_{H,V}(r')dr' = Z_{H,V}(r) - PIA_{H,V}(r) \quad (2)$$

where $Z'_{H,V}$ is the attenuated (i.e. measured) $Z_{H,V}$, $A_{H,V}$ is the (one-way) specific attenuation at H or V polarization (in dB km^{-1}), r is range (in km), and PIA_H and PIA_V are two-way path integrated horizontal and vertical attenuation (in dB), respectively. Similarly, measured differential reflectivity Z'_{DR} is given as

$$Z'_{DR}(r) = Z_{DR}(r) - 2\int_0^r A_{DP}(r')dr' = Z_{DR}(r) - PIA_{DP}(r) \quad (3)$$

where Z_{DR} is the intrinsic differential reflectivity (in dB), PIA_{DP} is the two-way path integrated attenuation (in dB), and A_{DP} is the specific differential attenuation (in dB km^{-1}):

$$A_{DP} = A_H - A_V \quad (4)$$

If attenuation can be accurately estimated, attenuation-corrected reflectivity and differential reflectivity can be obtained by solving (2) and (3) for $Z_H(r)$ and $Z_{DR}(r)$, respectively. A review of several attenuation correction techniques is provided in Park et al. (2005a); a brief explanation of the techniques used in this study is given below.

Early attempts to compensate for attenuation involved the use of single-polarization radar data and was outlined by the differential equations of Hitschfeld and Bordan (1954), wherein the following parameterization can be constructed:

$$A_H = aZ_h^{\,b} = a(10^{Z_H/10})^b \quad (5)$$

where A_H is in dB km^{-1}, Z_h is in mm^6 m^{-3}, and Z_H is in dBZ. This relation is often unstable and can be heavily affected by, among others, improper radar calibration and partial beam blockage. Using K_{DP} provided by dual-polarization weather radars, one can use a more stable approach,

whereby specific horizontal and differential attenuation can be estimated by the following parameterizations:

$$A_H = \alpha_H K_{DP}^{\beta_H} \tag{6}$$

$$A_{DP} = \alpha_{DP} K_{DP}^{\beta_{DP}} \tag{7}$$

where K_{DP} is in deg km^{-1}, α_H and α_{DP} are in dB deg^{-1}, and A_{DP} is in dB km^{-1}. The relations (6) and (7) are often assumed to be linear, which is approximately valid at most weather radar frequencies (Bringi et al. 1990; Jameson 1992; Park et al. 2005a). The coefficients in the above two relations must be supplied *a priori*, and they vary as a function of the DSD, temperature, and drop shape relation. Using data collected during 2005-2007 by a 2D-video disdrometer located in central Oklahoma (Cao et al. 2008; Cao and Zhang 2009) and scattering amplitudes from the T-matrix method [Waterman 1969; at 10°C, 0.0321 m wavelength, and using the drop size-shape relation from Brandes et al. (2002)], α_H and α_{DP} were calculated to be 0.313 and 0.0483, respectively. Hereafter, this specific attenuation – differential phase parameterization method is referred to as the "DP" method.

Another correction algorithm, termed the ZPHI method (Testud et al. 2000), constrains PIA_H by the total change in ϕ_{DP} along a radial through a rain cell. The attenuation is then apportioned according to the distribution of Z_H along the radial, making this technique significantly more stable than (5). A complete derivation is provided in Bringi and Chandrasekar (2001). ZPHI requires two *a priori* values – the coefficient in the A_H -K_{DP} relation (α_H; 6) and the exponent in the $A_H - Z_H$ relation (b; 5). In simulations at X-band performed by Park et al. (2005a), the former varied considerably with drop shape in the range 0.173-0.315 dB deg^{-1}, values similar to those obtained by Matrosov et al. (2002) and Anagnostou et al. (2004).

Comparing the ZPHI algorithm with the DP technique, Gorgucci and Chandrasekar (2005) found that the ZPHI algorithm generally performed better.

The ZPHI algorithm provides an estimate of the normalized intercept parameter, N_0^*, with which A_{DP} can be calculated according to the following:

$$A_{DP} = p\left[N_0^*\right]^{1-q} A_H{}^q \tag{8}$$

where, according to Testud et al. (2000), $p \approx 4.38$ and $q \approx 1.224$ at X-band.

The self-consistent with constraints (SCWC) method (Bringi et al. 2001) modifies ZPHI by attempting to find an optimal value of α_H by allowing α_H to vary within a predetermined range. For each α_H, a ϕ_{DP} profile is reconstructed using the following formula:

$$\phi_{DP}^{rec} = 2\int_{r_0}^{r} \frac{A_H(r',\alpha)}{\alpha_H} dr' \tag{9}$$

where r_0 is the starting range of the cell. The optimal α_H (i.e. α_{opt}) is the one that minimizes the difference between the observed ϕ_{DP} profile and the reconstructed ϕ_{DP}^{rec} profile. Estimated A_{DP} can be parameterized as follows:

$$A_{DP} = \gamma A_H \tag{10}$$

Park et al. (2005b) set the intrinsic Z_{DR} at the end of a ray to a value based on a constrained linear relationship between Z_{DR} and Z_H [ref. eq.(1) in Park et al. (2005b)], and the same relation is used in this paper. According to Park et al. (2005b), from this Z_{DR} constraint and the change in ϕ_{DP} from the starting (r_0) and ending (r_1) range of a cell, α_{opt} can be used to find the optimal γ in (10) as

$$\gamma_{opt} = \frac{1}{\alpha_{opt}} \frac{\left|Z_{DR}(r_1) - Z_{DR}^{'}(r_1)\right|}{\phi_{DP}(r_1) - \phi_{DP}(r_0)} \tag{11}$$

Tuttle and Rinehart (1983), using an X-band – S-band dual-wavelength radar, estimated PIA_H by the dual-wavelength ratio (hereafter, DWR), defined as the difference between the S-band and X-band horizontal reflectivity factor at the end of the cell. The pseudo-dual-frequency (PDF) method estimates PIA_H at the end of a ray by the DWR and apportions attenuation similarly to the ZPHI algorithm. The specific form used is that from Zhang et al. (2004), termed the adjusted Hitschfeld-Bordan method. Since the PDF method requires radar data from systems having two different frequencies and is highly dependent upon the assumption of Z_H being equal at S- and X-band, as well as free of hail contamination, it is used on the 29 May 2004 case (which is the only case in which the availability of a polarimetric S-band radar also allows for a comparison of other radar parameters).

A short overview of the main techniques, and a priori constants required for each technique, are given in Table 1. Note that attenuation correction, as it applies in this paper, is only an application of attenuation *estimates* to the observations. The corrections obtained herein assume that the precipitating media are characterized by rain. Hail can have various effects on the relationships between attenuation and radar measurements; the parameters in (5)-(7) may be significantly different in all rain than in hail or rain-hail mixtures. Since the imaginary component of the dielectric constant of ice is much lower than that of liquid water, attenuation by hail with low fractional water content tends to be much lower than that by rain. In addition, because the contribution of hail towards the measured K_{DP} tends to be small, the presence of hail may only minimally affect attenuation estimates using the correction methods in this paper (i.e. those that are based on the ϕ_{DP} data). However, attenuation by wet or melting hail may be quite appreciable in some situations (Ryzhkov et al. 2009). Unfortunately, some hail contamination is nearly unavoidable since many of the storms observed by UMass X-Pol have considerable

amounts and sizes of hail. In addition, large hail may occur within the nearest portion of the echoes (e.g. along the periphery of the mesocyclone of a supercell), so only performing attenuation estimation at ranges up to those where hail is present may all but prohibit the estimation of attenuation. Unfortunately, to estimate the locations of hail (via hydrometeor classification), one must correct for attenuation first. As a result, some of the attenuation estimates presented are contaminated by hail.

b. Hydrometeor classification

Fuzzy logic is a popular choice for hydrometeor classification for data at S-band (e.g. Zrnic et al. 2001; Liu and Chandrasekar 2000; Lim et al. 2005) and C-band (e.g. Keenan 2003; Marzano et al. 2006). Hydrometeor classification of X-band data using fuzzy logic is relatively new, though, with limited applications in the literature (e.g. Iwanami et al. 2007; Dolan and Rutledge 2009). The starting point of the hydrometeor classification algorithm used in this paper is from Park et al. (2009); the weights, inputs, and S-band membership functions are the same as those given by Park et al. (2009). A hybrid aggregation method, similar to that proposed and used by Lim et al. (2005), is used in this study:

$$RS_j = PS_{j\_ZH} \times \sum_{k \neq ZH} w_{j\_k} PS_{j\_k} \qquad (12)$$

where RS_j is the rule strength for hydrometeor class j, PS_{j_k} is the proposition strength of class j for input k, and w_{j_k} is the weight for class of j for input k.

Given the uncertainties in the establishment of membership functions, a relatively simple trapezoidal model is used. The membership functions are modifications based upon Park et al. (2009) and influenced by past work at S-band (Straka et al. 2000; Zrnic et al. 2001; Lim et al. 2005; Matrosov et al. 2006) and C-band (Marzano et al. 2006). One of the most significant

changes is to the membership functions that use K_{DP}; since K_{DP} scales very nearly (though, as a result of non-Rayleigh effects, not exactly or always consistently) with wavelength, K_{DP} through rain at X-band is approximately three times as large as at S-band. As in Park et al. (2009), the classification scheme actually uses LK_{DP} [defined as $LK_{DP} = 10\log(K_{DP})$ for $K_{DP} > 10^{-3}$ deg km^{-1}; - 40 otherwise] instead of K_{DP}; scattering calculations indicate that LK_{DP} exhibits considerably more linearity with Z_H (in dBZ) than does K_{DP}., which makes the LK_{DP}-Z_H two-parameter membership functions easier to describe. For the X-band membership functions for LK_{DP}, the parameters that describe the bounds of the membership functions are determined with the help of calculations using the disdrometer observations as well as idealized DSDs.

Resonance effects associated with non-Rayleigh scattering are likely to affect Z_H, Z_{DR}, and, to a lesser extent at X-band, ρ_{HV}. For example, calculating the scattering amplitudes using the T-matrix method for monodispersed DSDs of dry hail (0% fractional water) with 2 g m^{-3} ice water content, canting angle mean of 0° and standard deviation of 60° [calculated as in Jung et al. (2008)], and a fixed 0.75 axis ratio, reveals that the equivalent Z_H at X-band may differ significantly from that at S-band (e.g. 10-20 dBZ; Fig. 1b), an observation that has been known for many years (e.g. Atlas and Ludlam 1961). The scattering characteristics of hailstones are also sensitive to the fractional water content of the hailstones, as seen by comparing Figs. 1b-c (calculated for "wet" hail with 10% fractional water and 55.2° canting angle standard deviation). This is an important consideration since many have come to associate large hail with very high equivalent Z_H (i.e. >55 dBZ), a relationship that does not necessarily hold at X-band.

In the case of rain, the intrinsic Z_H and Z_{DR} at X-band is found to be slightly higher than at S-band (Fig. 1a), particularly for larger drops; Z_H values calculated using the aforementioned disdrometer observations are, on average, approximately 1-2 dBZ greater at X-band than at S-

band in rainrates exceeding 20 mm hr^{-1}. For DSDs that may characterize the "big drop" regime (for example, a series of monodispersed DSDs with drop diameters of 4-7 mm and concentrations of 0.01 - 1 m^{-3}), Z_H at X-band are often ~4 dBZ greater than at S-band. As such, the ranges of Z_H for rain and hail tend to have significantly greater overlap at X-band than at S-band, which reduces the power of Z_H to discriminate between hail and rain in hydrometeor classification at X-band.

In terms of Z_{DR}, Matrosov et al. (2006) found that there is little difference between S-band and X-band for DSDs characterized by small mean mass-weighted drop diameters (i.e. D_m < 2 mm), with X-band Z_{DR} increasing to beyond 0.3 dB above that at S-band for DSDs with larger mass-weighted drop diameters. Scattering calculations performed for this paper support this notion as well; Z_{DR} at X-band exceeds that at S-band by as much as ~15% (for drops of equivolume diameter of ~3 mm), and it is equivalent to or in excess of S-band Z_{DR} for all drop diameters (Fig. 1d). The behavior of Z_{DR} for hail is quite complicated (Fig. 1e-f); values at X-band can fluctuate on either side of 0 dB over relatively short hailstone diameter intervals, and the behavior of Z_{DR} can change significantly with different hailstone fractional water contents. The parameters that describe the X-band Z_{DR} membership functions, which are two-parameter functions with Z_H, were derived in the same way as those for K_{DP} (i.e. based on disdrometer observations and calculations of idealized DSDs).

Ryzhkov and Zrnic (2005) noted that resonance effects result in anomalously low ρ_{HV} at C-band compared to S-band; scattering calculations (not shown) using both the disdrometer observations and idealized/modeled DSDs reveal that ρ_{HV} at X-band is often slightly lower than at S-band, particularly for those DSDs that feature a greater concentration of large drops.

Since the radar was relatively close to the storms probed, most of the data used in this study were at an altitude well below the ambient freezing level; consequently, the output classifiers used in this study (Table 2) are limited to those expected in deep moist convection when the temperature is above freezing. In terms of classification system inputs, Z_H, Z_{DR}, ρ_{HV}, and LK_{DP} are used for all cases, as are texture parameters SD(Z_H) and SD(Φ_{DP}) defined below:

$$SD(Z_H) = \sqrt{\frac{\sum_{1km} (Z_H - mean(Z_H))^2}{n_Z}} \tag{13a}$$

$$SD(\Phi_{DP}) = \sqrt{\frac{\sum_{2km} (\Phi_{DP} - mean(\Phi_{DP}))^2}{n_\Phi}} \tag{13b}$$

where the mean in (13a) and (13b) are calculated through a 1 km and 2 km range centered on the range gate for which the parameter is calculated, respectively, and n_Z (n_Φ) equals the number of range gates in a 1 km (2 km) range. SD(Z_H) has been shown (Kessinger et al. 2001; Steiner and Smith 2002) to provide some value in distinguishing between meteorological targets and ground clutter / anomalous propagation; SD(Φ_{DP}) provides for a measure of the high-frequency variability of Φ_{DP} and, thus, is affected by large variations in δ with range; it is used to aid in discriminating meteorological from non-meteorological scatterers (Schuur et al. 2003; Park et al. 2009). Owing to the method by which K_{DP} is calculated, such data are unavailable within 750 m of edge of the cell along each radial. The parameters used to define each membership function are given in Table 3.

For the sake of brevity, and since others have examined them previously (e.g. Straka et al. 2000; Shuur et al. 2003; Kumjian and Ryzhkov 2008; Romine et al. 2008), polarimetric characteristics of different scatterers will not be discussed.

c. Radar and dataset characteristics

The mobile radar used in this study is a dual-polarization, X-band mobile radar developed at the University of Massachusetts – Amherst (UMass X-Pol) as a low-cost, highly-mobile observation platform (Fig. 2). Nearly every year since 2002, a team of graduate students and faculty from the University of Oklahoma's School of Meteorology and the University of Massachusetts have fielded the radar collecting data near supercells and related phenomena (e.g. Kramar et al. 2005; Bluestein et al. 2007a, 2007b). The radar antenna and components are mounted on a truck, similar to other mobile Doppler radars (e.g. Wurman et al. 1997; Bluestein and Pazmany 2000; Biggerstaff et al. 2005). More technical details on the radar can be found in Table 4 and in Junyent-Lopez (2003) and Pazmany et al. (2003).

The calculation of K_{DP} is made via linear regression over a 1.5 km range centered on the gate for which K_{DP} is being calculated, similar to Ryzhkov and Zrnic (1996) and Matrosov et al. (1999). It is necessary to remove δ from Φ_{DP} before calculating K_{DP}, and it is desirable to smooth the statistical fluctuations inherent in ϕ_{DP} data (Sachidananda and Zrnic 1986; Bringi et al. 1990). For the X-band data, Φ_{DP} data were processed using an iterative filtering method similar to that of Hubbert and Bringi (1995). This iterative method, however, cannot remove δ at either edge of the cell. Significant δ is apparent in only some of the datasets; at least a couple of the datasets contain appreciable δ along the right (often the south) side of the forward-flank updraft (nearly collocated with the Z_{DR} arc), which is probably due to non-Rayleigh scattering of large drops generated by size sorting (Kumjian and Ryzhkov 2009).

3. Results and Discussion

Three cases are described in detail below: one of significant attenuation in a tornadic supercell (29 May 2004), one of minor attenuation in a tornadic supercell (12 May 2004), and one of very significant attenuation in a squall line (21 May 2007).

a. 29-30 May 2004 – Single elevation-angle data with total attenuation in a tornadic supercell

On the afternoon and evening of 29 May 2004, a tornadic supercell traversed most of the state of Oklahoma. X-band data were collected approximately 13 km southeast of a strong tornado (Bluestein et al. 2007a), but the high-precipitation (HP; Moller et al. 1990) supercell resulted in massive attenuation and signal extinction through the storm (Fig. 3). Since the storm was approximately 80-95 km northwest of KOUN, this study makes use of KOUN data as a crude verification of intrinsic (unattenuated) Z_H and hydrometeor type. At a 0.0° elevation angle, the height of beam center from KOUN was approximately 500-600 m AGL for the part of the supercell that was sampled by the UMass X-Pol, slightly lower than the beam height (at 5.1° elevation angle) from the UMass X-Pol (~800m AGL). The gate spacing of the KOUN data collected on 29 May 2004 is 250 m, and the 3 dB cross-beam diameter at the designated range (80-95 km) is approximately 1.6-1.7 km; the gate spacing of the UMass X-Pol for this dataset is 150 m (oversampled every 15 m), and the 3 dB cross-beam diameter of the X-band data at the range of the tornado is approximately 300 m. Polarimetric data from the UMass X-Pol and KOUN radars are shown in Fig. 4. The ρ_{HV} data from this day are anomalously low for an unknown reason. Given the value of ρ_{HV} in hydrometeor classification, ρ_{HV} data for this case have been increased by 0.09, bringing ρ_{HV} in areas where rain is very likely to be occurring close into the 0.96-0.98 range. The mobile radar was scanning a relatively narrow sector at the time these

data were collected, and the sector sampled a part of the large, precipitation-filled rear-flank downdraft region of the supercell.

On many PPIs, the X-band radar signal experienced complete attenuation well before the back edge of the supercell. KOUN data were objectively-analyzed to the UMass X-Pol radar grid using a Barnes scheme (Barnes 1964) after efforts were made to align the KOUN and UMass X-Pol data in space. Differences in the times of available scans and heights of the beams from the two radars provide a source of error in this analysis. The estimated attenuation-corrected Z_H from the various techniques based on the 0055:37 UTC PPI are quite similar (Fig. 5). The α_H values of the SCWC technique calculated along each radial have a mean of 0.32, which is very close to the 0.313 used in the DP and ZPHI methods (i.e. the mean value obtained from aforementioned 2005-2007 disdrometer observations) and likely indicates that the propagation paths were characterized primarily of liquid precipitation. Since all single-radar corrections used in this study keep Z_H below approximately 55 dBZ, there is an obvious disparity when compared to the PDF technique that incorporates KOUN data (in which the reflectivity data are considerably higher than the corrected X-band data from single-radar techniques); the corrected Z_H from the PDF method (Fig. 5f) is 5-10 dBZ higher at the farther ranges (i.e. to the northwest of the tornado) than the results from the other techniques (Fig. 5c-e). As a result of the way by which ϕ_{DP} is processed, filtered ϕ_{DP} data are not available within at least 375 m of the edge of the cells (and often not within 500-600 m depending upon the specific case), so attenuation along the very front part of a radial may be underestimated (i.e. negative bias relative to the intrinsic field). This effect is particularly noticeable when heavy precipitation is located along the very edge of a cell.

The mean absolute error (MAE) was calculated, using KOUN as the reference, as

$$MAE = \frac{1}{n}\sum \left| Z_H - Z_H^S \right| \tag{14}$$

where Z_H^S is the radar reflectivity factor (in dBZ) from KOUN, Z_H is the corrected radar reflectivity factor (in dBZ) from the X-band radar, n is number of range bins used in the calculation of MAE, and the summation is performed over all range bins within the correction interval that are less than a particular threshold. Since the 55 dBZ threshold was used in the PDF technique to mark the lower bound of hail in the S-band data, and since the single-radar correction techniques are based on the assumption that precipitation is liquid rain, the MAE was calculated only at range bins for which $Z_H^S \leq 55$ dBZ.

In examining the differences between the KOUN-measured Z_H^S (Fig. 4a) and the X-band attenuation-corrected Z_H (Fig. 5), it is seen that Z_H^S generally exceeds Z_H. Differences in the resolution of the collected data and in the height of the radar volumes from the two radars, inhomogeneity within the radar resolution volumes (Zhang et al. 2002), and resonance effects are all possible reasons for the differences, though calibration differences may also contribute. Given the lower values of Z_H observed by the UMass X-Pol (both near the radar in the observed data and in the attenuation-corrected data), a bias was calculated from each attenuation-corrected dataset as

$$Bias = \frac{1}{n}\sum \left(Z_H - Z_H^S \right) \tag{15}$$

A bias-corrected MAE was calculated by subtracting the estimated bias from the X-band data as

$$BCMAE = \frac{1}{n}\sum \left| Z_H - Z_H^S - Bias \right| \tag{16}$$

The bias and bias-corrected MAE for all rays in the 0055:37 UTC scan are presented in Table 5.

The methodology used in this comparison (namely, the interpolation of lower-resolution KOUN data to the high-resolution mobile radar grid) contributes strongly to the MAE and BCMAE because the intrinsically higher-resolution nature of the mobile X-band radar data allows for the observation of finer-scale structures that are not present in the interpolated KOUN data. These structures increase the variability of the UMass X-Pol data relative to the KOUN data, contributing to the calculated MAE and BCMAE; even with a "perfect" attenuation-correction scheme, one would expect that BCMAE $\neq$ 0 solely owing to the resolution differences. In addition, as previously discussed, the intrinsic Z_H and Z_{DR} for a particular radar resolution volume may not be the same at X-band as they are at S-band owing to non-Rayleigh effects, *which means that MAE and BCMAE should not equal zero*.

The BCMAE based on the ZPHI technique, as in Gorgucci and Chandrasekar (2005), is lower than that estimated from the DP technique. Slightly lower is the BCMAE based on the SCWC technique, which should be an improvement over the ZPHI technique since the SCWC method is less sensitive to variability in the DSDs as a result of not having to prescribe a fixed α_H. Using different Z_H upper-range thresholds (i.e. comparing only those locations for which the Z_H values were less than the specified threshold) resulted in no change in relative performance of each technique. Similarly, changing the smoothing parameter, κ, of the Barnes analysis had little effect on the relative performance of each technique. From a qualitative standpoint, all methods yield corrections that appear realistic, and the results of the SCWC correction are selected for use in hydrometeor classification.

The differential attenuation-corrected estimates are compared in Fig. 6. For the most part, PIA_{DP} at the farthest ranges (immediately before signal extinction) is in the 4-6 dB range. Qualitatively, there is no apparent trend in Z_{DR} with range, save for the possible exception of the

technique associated with the ZPHI algorithm, which corrects less than the other techniques. This apparent underestimation of differential attenuation with the ZPHI method is associated with very high retrieved N_0^*, and further examination of the cause of this is ongoing. The qualitative error in Z_{DR} (i.e. MAE) was calculated but is not included because, from the nearest edge of the cell, X-band Z_{DR} is greater than Z_{DR}^S (Fig. 4c-d), and, since resonance effects are likely to affect the H and V channels differently for oblate precipitation particles at X-band, comparing Z_{DR} at S-band and X-band may be difficult. In addition, the $Z_{DR}^{'}$ data are only available with a relatively crude precision of 1 dB in this dataset.

With attenuation estimated (Figs. 5-6), one can more accurately interpret the suite of polarimetric products available from the UMass X-Pol radar. The most notable feature evident in the data is the tornado, characterized by the collocation of a weak echo minimum ($Z_H < 25$ dBZ), very low Z_{DR} of less than 1 dB, a strong cyclonic couplet in radial velocity (not shown), and very low ρ_{HV} (Fig. 4g-h). Such a characterization is consistent with the polarimetric tornado debris signature that has been observed with other polarimetric weather radars in the United States (e.g. Ryzhkov et al. 2005; Conway et al. 2007). The area of very low $Z_{DR}^{'}$ noted by Bluestein et al. (2007a) west of the tornado (Fig. 6a) is the result of strong differential attenuation, an artifact largely removed by the differential attenuation correction (Fig. 6b-d). High Z_H and Z_{DR} characterize the area between the radar and the tornado; visual observations corroborate very heavy precipitation, certainly enough so as to conceal the location of the tornado from observers near the radar. A band of $K_{DP} > 4$ deg km^{-1} (with local maxima exceeding 8 deg km^{-1}; Fig. 4f) nearly encircles the tornado, while K_{DP} of 0-1 deg km^{-1} characterizes the precipitation within approximately 8 km of the radar (i.e. south of a nearly east-west line at 47 km on the ordinate).

Hydrometeor type was estimated from the KOUN and attenuation-corrected X-band data (Fig. 7) using the results of the SCWC method. The X-band hydrometeor classification retrievals are similar to the KOUN classification, though differences are evident. For example, the region surrounding the tornado is classified as 'HR' (with no 'RH' in the UMass X-Pol data), while 'RA' and 'BD' are indicated in all classifications in the region 2-8 km northwest of the mobile radar (where the X-band K_{DP} is relatively low). The UMass X-Pol classifications show 'HR' in a ~1.5 km wide annulus around the tornado, though this region is thicker to the southwest through north of the tornado than in other areas. Significant reductions in ρ_{HV}, likely to reduce the accuracy of the classification, are noted beyond a range of approximately 13 km, and can be attributed to low SNR as the attenuated signal neared the system's noise floor. In areas of 'RH' in the KOUN classification, K_{DP} and Z_{DR} from the UMass X-Pol are relatively high for what is commonly thought to be associated with hail.

b. 12 May 2004 – Single-elevation angle with minor attenuation in a tornadic supercell

More than half a dozen tornadoes were produced by a tornadic supercell between the towns of Medicine Lodge and Harper in southwestern Kansas on the evening of 12 May 2004. Several of these tornadoes, including an F2 that went through the eastern side of Attica, Kansas, were probed by the X-band radar (Bluestein et al. 2007a). In situ observations of the 12 May 2004 supercell, in contrast to the supercell on 29 May 2004, indicated little in the way of significant rainfall in the RFD before and during the time of the Attica tornado. Large hail ~7 cm in diameter was experienced by one of the authors as he was 1-3 km north through west of the beginning path of the Attica tornado 5-10 minutes before the scans examined herein.

For comparison purposes, Fig. 8a-b contains the reflectivity imagery as seen from

KVNX, a WSR-88D located in northwestern Oklahoma, and from UMass X-Pol, at a time very near 0100 UTC. One obvious difference between the X-band and S-band data is the much higher reflectivity in the S-band data (Fig. 8a) compared to the X-band data (Fig. 8b), particularly near the longer ranges of the UMass X-Pol data to the northwest of the radar. The supercell that produced the Attica tornado was approximately 50 km north of KVNX; the beam height from the 0.5° elevation angle scan from KVNX was approximately 600 m AGL (neglecting changes in ground elevation). The mobile radar was situated approximately 4 km from two of the tornadoes produced by that supercell. Though the maximum range is considerably closer than that on 29-30 May 2004, there is very little change in ϕ_{DP} with range (Fig. 8c; i.e. $K_{DP} < 1°$ km^{-1}) in much of the X-band data. However, there appears to be more significant δ than was measured on 29 May 2004; some radials are not characterized by monotonically-increasing ϕ_{DP}, such as those indicated by the black ellipse in Fig. 8c. As a result, δ (or, more specifically, gradients of δ with range) effectively "contaminate" the K_{DP} field. As such, the iterative filtering method is not able to remove δ to estimate ϕ_{DP} properly, resulting in a negative change in ϕ_{DP} along some radials. It is also possible that resonance effects associated with scattering from very large hail are resulting in K_{DP} legitimately being negative.

With little change in ϕ_{DP} along each radial, estimated values of PIA_H and PIA_{DP} are rather small (and certainly much smaller than in the previous case). The DP, ZPHI (Fig. 8d), and SCWC techniques estimate maximum PIA_H on the order of 3-4 dBZ at the farthest range bins. The results of the correction using the SCWC technique are quite "streaky" as a result of radial-by-radial variability in the calculated α_{opt}. In addition, some lingering areas in which ϕ_{DP} decreases with range (i.e. $K_{DP} < 0$ deg km^{-1}) near the front edge of the cell yield an incorrect calculation of α_{opt}. The techniques that utilize the entire range profile of ϕ_{DP} are problematic

when ϕ_{DP} does not monotonically increase with range. As such, the DP technique actually estimates $A_H < 0$ dBZ km^{-1} near the front of the cell, which is not physically realistic. With little appreciable change in ϕ_{DP} with range, estimates of differential attenuation are minimal (largely < 1 dB) and are not shown. In this case, which features areas of very small and sometimes negative K_{DP}, the most reasonable results (e.g. those that do not estimate $A_H < 0$ dBZ km^{-1}) are obtained with the ZPHI method, and these results are used in the hydrometeor classification.

A couple of noteworthy features (Fig. 9) include a vortex signature perhaps most evident in the Z_{DR} and ρ_{HV} data, centered approximately 4 km west of the radar location. A quasi-circular region of $\rho_{HV} < 0.7$ of diameter ~1 km is associated with $-2 < Z_{DR} < 0.5$, with an inner region of approximately 150 m characterized by $Z_{DR} < -4$ dB. An annulus of maximum Z_H near 30-35 dBZ is collocated with the significant Z_{DR} and ρ_{HV} depressions, marking the core of the tornado and making up the debris signature noted in other analyses of tornadoes using dual-polarized radar data (Ryzhkov et al. 2005; Bluestein et al. 2007b; Kumjian and Ryzhkov 2008). As noted by Bluestein et al. (2007b), the inner ring of higher Z_H is likely the result of debris centrifuged radially outward from the center of the vortex (Snow 1984; Dowell et al. 2005), while the outer spiral bands evident in the Z_H data are composed of meteorological hydrometeors and other scatterers.

Along the south side of the forward flank downdraft (FFD), there is a second prominent signature evident in the Z_{DR} data (Fig. 9a). Coincident with Z_H of 20-40 dBZ is a band of high Z_{DR} (i.e. 5-6 dB) approximately 500 m wide that appears along the inflow (i.e. south) side of the FFD. The location and range of polarimetric variables within this band resemble the Z_{DR} arc (Kumjian and Ryzhkov 2008; Romine et al. 2008), a feature that may arise from drop size sorting in the presence of strong low-level vertical wind shear (Kumjian and Ryzhkov 2009). If

this process is occurring in this particular case, the 'BD' hydrometeor type should comprise the band. The Z_{DR} arc is even more evident at 0121:44 UTC (Fig. 10b), having a width of approximately 500 m and stretching through the hook echo; indeed, the hydrometeor classification for this scan (Fig. 10e) is 'BD' in this part of the storm, though 'GC/AP' is also erroneously assigned. The area of precipitation deeper into the FFD (i.e. northwest of the radar by 3-6 km) is characterized by relatively low ρ_{HV}, Z_H of 45-55 dBZ, and Z_{DR} of 3-4 dB, indicative of either heavy rain or a rain-hail mix (the relatively low ρ_{HV} is evidence for the latter). This appears to be a case where hail may be occurring even in the presence of high Z_{DR}.

At 0121:44 UTC (Fig. 10), along the right side of the FFD (i.e. on the side nearest the low-level inflow, or the southeast side at this time) and near the inside portion of the hook echo, ρ_{HV} is low in magnitude and is characterized by high spatial variability (Fig. 10c), Z_{DR} is characterized by high spatial variability (Fig. 10b), and Z_H is in the 15-40 dBZ range (Fig. 10a); this signature is located adjacent to, and on the low-level inflow side of, the Z_{DR} arc. It is very possible that such a signature is the result of dust, insects, and other non-meteorological scatterers being ingested into the updraft on surface inflow winds (Kumjian and Ryzhkov 2008). This signature is present but less evident at 0101:23 UTC, marked mostly by very low ρ_{HV} (e.g. lower than 0.65; Fig. 9b) and Z_H between 15 and 25 dBZ (Fig. 8d).

Hydrometeor type retrievals at 0101:23 UTC based on the corrected fields from the various techniques are, not surprisingly given the minimal attenuation, quite similar; the retrieval using the ZPHI method is seen in Fig. 9d. In general, the corrections yield a classification consisting of a 'HR' in the FFD north of the tornado, a relatively narrow ribbon of 'BD' on the south side of the FFD, an inflow notch consisting of 'BS', and a tornado core that is primarily classified as 'GC/AP' (i.e. nonmeteorological). From the first-hand experience of one of the

authors, extremely large hail may have been falling closer to the tornado than the hydrometeor classification results indicate. As noted previously (Fig. 8a-b), since Z_H^S was much greater than the X-band Z_H to the north of the tornado (in the southwest part of the FFD), and since the ϕ_{DP} profile does not change appreciably with range (i.e. the magnitude of K_{DP} is very small), large hail may be common in this part of the storm (Fig. 1). The lack of 'RH' is noteable in these data; it is likely that the large Z_{DR} contributed to the assignment of 'BD' over 'RH', even if the "true" hydrometeor type may have been large hail (with the relatively large difference between S-band and X-band ZH and the relatively low KDP) mixed with a low number concentration of large rain drops (and associated large ZDR), perhaps shed from the water-coated hailstones. The possibility exists that attenuation through the observed hail actually was significant, and the relatively low observed reflectivity may have been the result of the schemes assuming an all-rain medium. These results support the need to better establish the membership functions for hail at X-band.

Owing to the unavailability of several inputs to the classification scheme (i.e. K_{DP}, SD(Z_H) and SD(ϕ_{DP})) as a result of the proximity of the Z_{DR} arc to the very front edge of the cell, the quality of the classification is likely to be significantly reduced in this area. There is at least one range-related feature in Fig. 9 that is worth mentioning – the cessation of 'HR' and the appearance of more widespread 'GC/AP' towards the top of Fig. 9d (between a range of about 6.5 – 7 km north of the radar). For similar reasons why the Z_{DR} arc may not always be properly classified, this range-related feature can be attributed to the reduced number of inputs available near the edges of the radar data. Unfortunately, classification of narrow echoes is either not possible or is of reduced quality as a result of a reduced number of available inputs.

c. 21 May 2007 – Volumetric data with total attenuation in severe squall line

The X-band mobile radar also sampled a quasi-linear convective system (QLCS) that developed across parts of the Texas panhandle on 21 May 2007 (Fig. 11). As on 29-30 May 2004, there was complete attenuation of the signal over very short distances; SNR dropped below 10 dB over through-storm distances as short as 8 km. Given the orientation of the QLCS relative to KAMA, some attenuation is also likely to have occurred in the S-band data. Fortunately, the mobile radar data largely encompass the parts of the convective line that was nearest KAMA; unfortunately, KAMA is a single-polarization radar, so correcting for attenuation in these data is not feasible.

The majority of the squall line sampled by the X-band radar was located approximately 65-96 km to the northeast of KAMA (Fig. 12). At such a range, the height of the beam center from the 0.5° elevation angle scan from KAMA was approximately 0.8 – 1.4 km AGL; the X-band radar's beam, at 2.6° elevation angle and slant ranges of 20 - 35 km, was 0.9 – 1.4 km AGL. The 3 dB cross-beam diameters from KAMA and UMass X-Pol at the considered ranges were 1.1 – 1.7 km and 0.4 – 0.8 km, and data from the S-band and X-band radars are available every 1 km and 60 m in range, respectively. Several areas of K_{DP} of 10-11 deg km^{-1} are noted within the convective system, the result of very high rain-rates and water content within the leading convective region; significant attenuation are expected given the such high K_{DP}.

The attenuation estimates and corrections for the 2338:51 UTC scan are mostly 30-32 dBZ; Fig. 13c contains the results from the ZPHI technique. The results from the SCWC method are not shown since there is large radial-to-radial variability, and a plot of some of the observed versus reconstructed ϕ_{DP} profiles reveals that some radials are characterized by positive increases in ϕ_{DP} with range along the leading edge of the QLCS even in areas of relatively low Z_H. The

signal penetrates considerably farther into the convection in some parts of the QLCS than in other adjacent parts; these relatively narrow zones mark areas in which signal attenuation was weaker. Though the exact reasons for this are not known, it is likely that the DSDs in these narrow zones differed from those in adjacent areas of the QLCS, allowing the signal to penetrate deeper into the heavy convection before complete attenuation. Spatial heterogeneity of DSDs in severe convection evidenced by differing attenuation rates through volumes characterized by similar values of Z_H is also seen in other UMass X-Pol supercell datasets when comparing, for example, the RFD and FFD of some supercells (e.g. in Fig. 3b, it is seen that Z_H profiles for rays passing through the FFD tend to be characterized by higher Z_H over longer distances than rays passing through the rear-flank downdraft near the tornado, even though nearly all rays experience extinction through the storm).

There is a sharp gradient in Z_{DR} near the rear of the observed data, beyond which Z_{DR} decreases to less than -4 dB; Fig. 13e contains the results of differential attenuation correction using the DP method. There are differences among the results of the differential attenuation correction techniques, largely at the ranges beyond which the signal is heavily attenuated and the signal-to-noise ratio (not shown) is low. In general, the correction based on the SCWC method was significantly greater than those based on the DP and ZPHI techniques, particularly near the end of the rays, where PIA_{DP} estimated from SCWC is more than 2-3 dB greater than that estimated using the DP and ZPHI methods. Near the end of the rays that are most normal to the squall line, differential attenuation correction still results in $Z_{DR} < 0$ dB (Fig. 13e) coincident with $Z_H > 45$ dBZ. Although the presence of hail may be inferred from such data, it is quite possible that the depressed Z_{DR} values are an artifact of very low SNR.

Hydrometeor types estimated (e.g. Fig. 14 using the ZPHI correction) from the

corrections of the various techniques indicate primarily 'HR' several kilometers rearward of the leading edge of the squall line, and some deeper zones of 'BD' at the leading edge of the cell for those radials that penetrate farther into the squall line. In other words, the 'RA' classifications are not indicated until several kilometers into the convection, for the most part, in those radials that were also able to extend farther into the convection before signal extinction occurred. The 'BD' classification near the leading edge of the squall line is reasonable in that primarily only the larger drops have a high enough terminal velocity to fall through the convective updraft. Again, the radar signal completely attenuates over such short distances that hydrometeor classification in some parts of the convection is hampered by the unavailability of K_{DP} as a result of the previously-mentioned processing of ϕ_{DP} and calculation of K_{DP}. The proliferation of the 'GC/AP' classification near the end of most rays is the result of low ρ_{HV} in the presence of low SNR caused by the severe attenuation; much of this misclassified area is removed if the data are masked by a higher (e.g. 20 dB) SNR threshold.

4. Conclusions

In most instances, attenuation and differential attenuation must be accounted for in any quantitative interpretation of X-band radar data of appreciable precipitation. In this paper, several correction techniques were examined and applied to mobile, X-band radar data of severe convection collected. It is emphasized that, although attenuation can be estimated, and its effects on the Z_H and Z_{DR} fields compensated, little can be done after the signal drops to near the noise floor. As such, the ability to observe deep moist convection with intense, attenuating precipitation cores beyond the scale of ~10-15 km in radial extent with a single X-band weather radar can be severely limited. Though the data collected by the UMass X-Pol and similar X-

band mobile radars provide superior resolution when compared to many other weather radar systems used in the United States, the extremely severe attenuation that occurs in some convective storms is prohibitive to data collection efforts. Fortunately, not all storms produce attenuation that is as severe as was observed on 29 May 2004 and 21 May 2007.

On 29 May 2004, the SCWC technique generally provided the best match to S-band, WSR-88D data, as well it should be since δ was negligible or removed in the processing of ϕ_{DP}. In contrast, the inability to remove areas of negative K_{DP} (i.e. ranges through which ϕ_{DP} decreases with range) on 12 May 2004 resulted in a streaky, over-estimation of attenuation using the SCWC method. In general, the SCWC technique tended to over-correct for attenuation for any radial in which ϕ_{DP} decreased with range (as occurs when gradients in δ are not removed or, possibly, when hail of certain sizes and fractional water concentrations are present), even if the decrease occurs over relatively short distances. As such, when SCWC is employed, the entire ray is affected when gradients in δ are present anywhere along the ray, or when the intrinsic K_{DP} for a particular resolution volume is negative (which can happen in hail). The ZPHI technique, however, is only affected by δ when it is present at the starting and ending range of the cell.

The PDF technique retained subtle structures in the Z_H field, but it tended to provide a correction that was the largest amongst the suite of techniques, the result of assuming that the intrinsic, X-band Z_H at the end of each radial was the same as the observed S-band Z_H. In the cases of total attenuation (e.g. 29 May 2004 and 21 May 2007) the farthest range of each ray in the X-band data tended to fall in an area characterized by $Z_H^S > 60$ dBZ. It is quite possible that the end of rays that experienced total attenuation occurred where hail was present, which would likely result in Z_H^S higher than the intrinsic X-band Z_H. In addition, for most of the data from the UMass X-Pol, the available S-band radars sampled different volumes then the X-Pol owing to

significant differences in, among others, radar resolution volume size and height above ground level. As such, this technique is often not suitable for use with data that have been collected by the UMass X-Pol during the annual spring field campaigns.

The results of the hydrometeor classification from the only case for which polarimetric radar data from another radar are available (i.e. 29 May 2004) appear to be positive, though the retrieved classifications from the two radars do not match completely. Most significantly, and as was seen on 12 May 2004 as well, the scheme did not assign the 'RH' class over as large an area as was observed by KOUN (on 29 May 2004) or by limited ground observations (12 May 2004). In the former case, attenuation-corrected Z_{DR} remained relatively high (>3 dB) in areas for which the retrieved class from KOUN was 'RH'; in the latter case, even the observed Z_{DR} was high (> 3 dB) in areas that may have contained very large hail. In both cases, though, the center of the tornadoes was correctly classified as being non-meteorological. The further refinement of the membership functions and weights used in the classification scheme is very important.

Future field campaigns will seek to collect X-band polarimetric data of severe convection while nearly collocated with an S-band polarimetric radar (such as KOUN). Such a dataset would allow for a more accurate "tuning" of the X-band membership functions used in the hydrometeor classification system since it would remove some of the analysis errors that arise from spatial and temporal differences in the data from the two radars. It seems prudent to examine a method by which to estimate X-band data using S-band data, similar to what was done by Chandrasekar et al. (2006); doing so may remove some of the limitations and assumptions of attempting to use S-band data to verify X-band attenuation estimates. A proper correction of ρ_{HV} for noise (Schuur et al. 2003) should help mitigate one problem often present in the UMass X-Pol data – namely, a significant reduction in ρ_{HV} observed near the end of rays that experience

significant attenuation.

Acknowledgments

The authors extend their appreciation to Robert Palmer for providing useful discussion and feedback while serving as a member of the first author's Master's Thesis committee at the University of Oklahoma. The authors also thank Alexander Ryzhkov and Matthew Kumjian for insight and help with parts of this work, as well as Andrew Pazmany, Francesc Junyent-Lopez, Kery Hardwick, Michael French, and Matthew Kramar for their effort in the collection and processing of some of the X-band mobile radar data used in this project. The helpful comments and critiques from three anonymous reviewers also improved this paper. This work was supported by NSF grants ATM-0241037, ATM-0637148, and ATM-0608168 awarded to the University of Oklahoma and ATM-0242166 and ATM-0641201 awarded to the University of Massachusetts.

References

Anagnostou, E. N., M. N. Anagnostou, W. F. Krajewski, A. Kruger, and B. J. Miriovsky, 2004: High-resolution rainfall estimation from X-band polarimetric radar measurements. *J. Hydrometeor.*, **5,** 110-128.

Atlas, D., and F. H. Ludlam, 1961: Multi-wavelength radar reflectivity of hailstorms. *Quart. J. Roy. Meteor. Soc.*, **87,** 523-534.

Barnes, S. L., 1964: A technique for maximizing details in numerical weather map analysis. *J. Appl. Meteor.,* **3,** 396–409

Biggerstaff, M. I., and Coauthors, 2005: The Shared Mobile Atmospheric Research and

Teaching Radar: A collaboration to enhance research and teaching. *Bull. Amer. Meteor. Soc.*, **86,** 1263-1274.

Bluestein, H. B., and A. L. Pazmany, 2000: Observations of tornadoes and other convective phenomena with a mobile, 3-mm wavelength, Doppler radar: The spring 1999 field experiment. *Bull. Amer. Meteor. Soc.*, **81,** 2939-2951.

——, M. M. French, R. L. Tanamachi, S. Frasier, K. Hardwick, F. Junyent, and A. L. Pazmany, 2007a: Close-range observations of tornadoes in supercells made with a dual-polarization, X-band, mobile Doppler radar. *Mon. Wea. Rev.*, **135,** 1522-1543.

——, C. C. Weiss, M. M. French, E. M. Holthaus, R. L. Tanamachi, S. Frasier, and A. L. Pazmany, 2007b: The structure of tornadoes near Attica, Kansas, on 12 May 2004: High-resolution, mobile, Doppler radar observations. *Mon. Wea. Rev.*, **135,** 475-506.

Brandes, E. A., 1978: Mesocyclone evolution and tornadogenesis: Some observations. *Mon. Wea. Rev.*, **106,** 995-1011.

——, G. Zhang, and J. Vivekanandan, 2002: Experiments in rainfall estimation with a polarimetric radar in a subtropical environment. *J. Atmos. Meteor.*, **41,** 674-685.

Bringi, V. N., V. Chandrasekar, N. Balakrishnan, and D. S. Zrnic, 1990: An examination of propagation effects in rainfall on radar measurements at microwave frequencies. *J. Atmos. Oceanic Technol.*, **7,** 829-840.

——, and ——, 2001: *Polarimetric Doppler Weather Radar: Principle and Applications.* Cambridge University Press, 636 pp.

——, T. D. Keenan, and V. Chandrasekar, 2001: Correcting C-band radar reflectivity and differential reflectivity data for rain attenuation: A self-consistent method with constraints. *IEEE Trans. Geosci. Remote Sens.*, **39,** 1906-1915.

Cao, Q., G. Zhang, E. Brandes, T. Schuur, A. Ryzhkov, and K. Ikeda, 2008: Analysis of video disdrometer and polarimetric radar data to characterize rain microphysics in Oklahoma. *J. Appl. Meteor. Climatol.*, **47,** 2238-2255.

Cao, Q., and G. Zhang, 2009: Errors in estimating raindrop size distribution parameters: A study based on simulation and real data. *J. Appl. Meteor. Climat.*, **48,** 406-425.

Chandrasekar, V., S. Lim, and E. Gorgucci, 2006: Simulation of X-band Rainfall Observations from S-band Radar Data. *J. Atmos. Oceanic Technol.,* **23,** 1195-1205.

Conway, J. W., A. V. Ryzhkov, E. D. Mitchell, P. Zhang, L. Venkatramani, J. L. Alford, and D. Nelson, 2007: Examination of tornadic signatures observed at very close range using simultaneous dual-polarization radar at C band. Preprints, *33rd Conference on Radar Meteorology*, Cairns, Queensland, American Meteorological Society, P10.12.

Dolan, B., and S. A. Rutledge, 2009: A theory-based hydrometeor identification algorithm for X-band polarimetric radars. *J. Atmos. Oceanic Technol.,* **26,** 2071-2088.

Dowell, D. C., and H. B. Bluestein, 1997: The Arcadia, Oklahoma, storm of 17 May 1981: Analysis of a supercell during tornadogenesis. *Mon. Wea. Rev.*, **125,** 2562-2582.

——, C. R. Alexander, J. M. Wurman, and L. J. Wicker, 2005: Centrifuging of hydrometeors and debris in tornadoes: Radar-reflectivity patterns and wind-measurement errors. *Mon. Wea. Rev.*, **133,** 1501-1524.

Gorgucci, E., and V. Chandrasekar, 2005: Evaluation of attenuation correction methodology for dual-polarization radars: Application to X-band systems. *J. Atmos. Oceanic Technol.*, **22,** 1195-1206.

Hitschfeld, W., and J. Bordan, 1954: Errors inherent in the radar measurement of rainfall at attenuation wavelengths. *J. Atmos. Sci.*, **11,** 58-67.

Hubbert, J., and V. N. Bringi, 1995: An iterative filtering technique for the analysis of copolar differential phase and dual-frequency radar measurements. *J. Atmos. Oceanic Technol.*, **12,** 643-648.

Iwanami, K., R. Misumi, M. Maki, T. Wakayama, K. Hata, and S. Watanabe, 2001: Development of a multiparameter radar system on mobile platform. Preprints, *30th International Conference on Radar Meteorology*, Munich, Germany, American Meteorological Society, 104-106.

——, K. Kusunoki, N. Orikasa, M. Maki, R. Misumi, and M. Murakami, 2007: Hydrometeor type classification in winter clouds using X-band polarimetric radar measurements -- comparison of X-band polarimetric radar data with in-situ measurements by HYVIS. Preprints, *33rd Conference on Radar Meteorology*, Cairns, Queensland, American Meteorological Society, P10.11.

Jameson, A. R., 1992: The effect of temperature on attenuation-correction schemes in rain using polarization propagation differential phase shift. *J. Appl. Meteor.*, **31,** 1106-1118.

Jung, Y., G. Zhang, and M. Xue, 2008: Assimilation of Simulated Polarimetric Radar Data for a Convective Storm Using the Ensemble Kalman Filter. Part I: Observation Operators for Reflectivity and Polarimetric Variables. *Mon. Wea. Rev.*, **136**, 2228-2245.

Junyent-Lopez, F. J., 2003: The design, development, and initial field deployment of an X-band polarimetric Doppler weather radar. M. S. thesis, Electrical and Computer Engineering, University of Massachusetts Amherst, 120 pp.

Keenan, T., 2003: Hydrometeor classification with C-band polarimetric radar. *Aust. Meteor. Mag.*, **51,** 23-31.

Kessinger, C., S. M. Ellis, and J. Van Andel, 2001: NEXRAD data quality: The AP clutter

mitigation scheme. Preprints, *30th International Conference on Radar Meteorology*, Munich, Germany, 707-709.

Kramar, M. R., H. B. Bluestein, A. L. Pazmany, and J. D. Tuttle, 2005: The "Owl Horn" radar signature in developing Southern Plains supercells. *Mon. Wea. Rev.*, **133,** 2608-2634.

Kumjian, M. R., and A. V. Ryzhkov, 2008: Polarimetric signatures in supercell thunderstorms. *J. Appl. Met.*, **47,** 1940-1961.

Kumjian, M. R., and A. V. Ryzhkov, 2009: Storm-relative helicity revealed from polarimetric radar measurements. *J. Atmos. Sci.*, **66,** 667-685.

Lemon, L. R., and C. A. Doswell, 1979: Severe thunderstorm evolution and mesocyclone structure as related to tornadogenesis. *Mon. Wea. Rev.*, **107,** 1184-1197.

Lim, S., V. Chandrasekar, and V. N. Bringi, 2005: Hydrometeor classification system using dual-polarization radar measurements: Model improvements and in situ verification. *IEEE Trans. Geosci. Remote Sens.*, **43,** 792-801.

Liu, H., and V. Chandrasekar, 2000: Classification of hydrometeors based on polarimetric radar measurements: Development of fuzzy logic and neuro-fuzzy systems, and in situ verification. *J. Atmos. Oceanic Technol.*, **17,** 140-164.

Matrosov, S. Y., R. A. Kropfli, R. F. Reinking, and B. E. Martner, 1999: Prospects for measuring rainfall using propagation differential phase in X- and Ka-radar bands. *J. Appl. Meteor.*, **38,** 766-776.

——, K. A. Clark, B. E. Martner, and A. Tokay, 2002: X-band polarimetric radar measurements of rainfall. *J. Appl. Meteor.*, **41,** 941-952.

——, R. Cifelli, P. C. Kennedy, S. W. Nesbitt, S. A. Rutledge, V. N. Bringi, and B. E. Martner, 2006: A comparative study of rainfall retrievals based on specific differential phase shifts

at X- and S-band radar frequencies. *J. Atmos. Oceanic Technol.*, **23,** 952-963.

Marzano, F. S., and D. Scaranari, M. Celano, P. P. Alberoni, G. Vulpiani, and M. Montopoli, 2006: Hydrometeor classification from dual-polarized weather radar: extending fuzzy logic from S-band to C-band. *Advances in Geosciences,* **7,** 109-114.

Moller, A. R., C. A. Doswell, and R. Przybylinski, 1990: High-precipitation supercells: A conceptual model and documentation. Preprints, *16th Conference on Severe Local Storms*, Kananaskis Park, Alberta, American Meteorological Society, 52-57.

Park, S. G., V. N. Bringi, V. Chandrasekar, M. Maki, and K. Iwanami, 2005a: Correction of radar reflectivity and differential reflectivity for rain attenuation at X band. Part I: Theoretical and empirical basis. *J. Atmos. Oceanic Technol.*, **22,** 1621-1632.

——, M. Maki, K. Iwanami, V. N. Bringi, and V. Chandrasekar, 2005b: Correction of radar reflectivity and differential reflectivity for rain attenuation at X band. Part II: Evaluation and application. *J. Atmos. Oceanic Technol.*, **22,** 1633-1655.

Park, H., A. V. Ryzhkov, D. S. Zrnic, and K. Kim, 2009: The Hydrometeor Classification Algorithm for the Polarimetric WSR-88D: Description and Application to an MCS. *Wea. Forecasting*, **24,** 730-748.

Pazmany, A. L., F. J. Lopez, H. B. Bluestein, and M. Kramar, 2003: Quantitative rain measurements with a mobile, X-band, polarimetric Doppler radar. Preprints, *31st Conference on Radar Meteorology*, Seattle, WA, American Meteorological Society, 858-859.

Romine, G. S., D. W. Burgess, and R. B. Wilhelmson, 2008: A dual-polarization-radar-based assessment of the 8 May 2003 Oklahoma City area tornadic supercell. *Mon. Wea. Rev.,* **136,** 2849-2870.

Ryzhkov, A. V., and D. S. Zrnic, 1996: Assessment of rainfall measurement that uses specific differential phase. *J. Appl. Meteor.*, **35,** 2080-2090.

——, and ——, 2005: Radar polarimetry at S, C, and X bands: Comparative analysis and operational implications. Preprints, *32nd Conference on Radar Meteorology*, Albuquerque, New Mexico, American Meteorological Society, 9R.3.

——, T. J. Schuur, D. W. Burgess, and D. S. Zrnic, 2005: Polarimetric tornado detection. *J. Appl. Meteor.*, **44,** 557-570.

——, and Coauthors, 2007a: Comparison of polarimetric algorithms for hydrometeor classification at S and C bands. Preprints, *33rd Conference on Radar Meteorology*, Cairns, Queensland, American Meteorological Society, 10.13.

——, S. Ganson, A. Khain, M. Pinsky, and A. Pokrovsky, 2009: Polarimetric characteristics of melting hail at S and C bands. Preprints, *34th Conference on Radar Meteorology*, Williamsburg, Virginia, American Meteorological Society, 4A.6.

Sachidananda, M., and D. S. Zrnic, 1986: Differential propagation phase shift and rainfall rate estimation. *Radio Sci.*, **21,** 235-247.

Schuur, T. J., A. V. Ryzhkov, P. L. Heinselman, D. S. Zrnic, D. W. Burgess, and K. A. Scharfenberg, 2003: Observations and classification of echoes with the polarimetric WSR-88D radar. National Severe Storms Laboratory Rep., 46 pp.

Smyth, T. J., and A. J. Illingworth, 1998: Correction for attenuation of radar reflectivity using polarization data. *Quart. J. Roy. Meteor. Soc.*, **124,** 2393-2415.

Snow, J. T., 1984: On the formation of particle sheaths in columnar vortices. *J. Atmos. Sci.*, **41,** 2477-2491.

Steiner, M., and J. Smith, 2002: Use of three-dimensional reflectivity structure for automated

detection and removal of nonprecipitating echoes in radar data. *J. Atmos. Oceanic Technol.*, **19,** 673-686.

Straka, J. M., Zrnic, D. S., and A. V. Ryzhkov, 2000: Bulk hydrometeor classification and quantification using polarimetric radar data: Synthesis of relations. *J. Appl. Meteor.*, **39,** 1341-1372.

Testud, J., E. Le Bouar, E. Obligis, and M. Ali-Mehenni, 2000: The rain profiling algorithm applied to polarimetric weather radar. *J. Atmos. Oceanic Technol.*, **17,** 332-356.

Tuttle, J. D., and R. E. Rinehart, 1983: Attenuation correction in dual-wavelength analyses. *J. Appl. Meteor.*, **22,** 1914-1921.

Vivekanandan, J., S. M. Ellis, R. Oye, D. S. Zrnic, A. V. Ryzhkov, and J. Straka, 1999: Cloud microphysics retrieval using S-band dual-polarization radar measurements. *Bull. Amer. Meteor. Soc.*, **80,** 381-388.

——, G. Zhang, and E. Brandes, 2004: Polarimetric radar estimators based on a constrained gamma drop size distribution model. *J. Appl. Meteor.*, **43,** 217-230.

Waterman, P. C., 1969: Scattering by dielectric obstacles. *Alta Frequenza*, (Speciale), 348-352.

Wicker, L. J., and R. B. Wilhelmson, 1995: Simulation and analysis of tornado development and decay within a three-dimensional supercell thunderstorm. *J. Atmos. Sci.*, **52,** 2675-2703.

Wurman, J., J. M. Straka, E. Rasmussen, M. Randall, and A. Zahrai, 1997: Design and deployment of a portable, pencil-beam, pulsed, 3-cm Doppler radar. *J. Atmos. Oceanic Technol.*, **14,** 1502-1512.

Zhang, G., J. Vivekanandan, and E. A. Brandes, 2002: Effects of random inhomogeneity on radar measurements and rain rate estimation. *IEEE Trans. Geosci. Remote Sens.,* **40**, 223-227.

Zhang, G., J. Vivekanandan, and M. K. Politovich, 2004: Radar/radiometer combination to retrieve cloud characteristics for icing detection. Preprints, *11th Conference on Aviation, Range, and Aerospace*, Hyannis, MA, American Meteorological Society, P6.6.

Zrnic, D. S., A. V. Ryzhkov, J. Straka, Y. Liu, and J. Vivekanandan, 2001: Testing a procedure for automatic classification of hydrometeor types. *J. Atmos. Oceanic Technol.*, **18,** 892-913.

List of figures

Fig. 1. A comparison of equivalent Z_H in (a) rain, (b) hail with 0% fractional water (FW; "dry hail"), and (c) hail with 10% fractional water content ("wet hail"); ZDR in (d) rain, (e) dry hail, and (f) wet hail; K_{DP} in (g) rain, (h) dry hail, and (i) wet hail as a function of particle diameter in a monodispersed DSD. The solid, long dashed, and short dashed curves represent the solutions for 10.7 cm, 5 cm, and 3.2 cm wavelength radars, respectively, as a function of equivolume diameter. The values for rain were calculated for 10°C, mean canting angle and canting angle standard deviation of 0°, and with liquid water content of 10 g m^{-3}. The values for dry hail (i.e. no fractional water content) were calculated using ice content of 2 g m^{-3}, 0° mean canting angle, and 60° canting angle standard deviation [calculated from Jung et al. (2008)]. The values for the wet hail are the same as for the dry hail, except with a 55.2° canting angle standard deviation. The drop size-shape relation for rain is the same as described by Brandes et al. (2002).

Fig. 2. Photograph of the UMass X-Pol in the spring of 2007. (Photograph courtesy of J. Snyder)

Fig. 3. A comparison of (a) 0.0° elevation angle data from KOUN and (b) 5.1° elevation angle data from UMass X-Pol valid 0044 UTC on 30 May 2004. Axes labels are relative to KOUN.

Fig. 4. $Z_H^{'}$ (a-b), $Z_{DR}^{'}$ (c-d), $3\times K_{DP}$ and K_{DP} (e-f), and ρ_{HV} (g-h) from KOUN (0.0°) and UMass X-Pol (5.1°), respectively, at approximately 0055 UTC on the evening of 29 May 2004. Note that K_{DP} for KOUN (e) has been scaled upward by a factor of 3. Axes labels relative to KOUN, and the black lines denote the approximate sector scanned by the UMass X-Pol.

Fig. 5. UMass X-Pol (a) ϕ_{DP}, (b) $Z_H^{'}$, and attenuation-corrected Z_H using the (c) DP, (d) ZPHI, (e) SCWC, and (f) PDF techniques from 0055:37 UTC on 30 May 2004 at an elevation angle of 5.1°.

Fig. 6. UMass X-Pol (a) $Z_{DR}^{'}$ and attenuation-corrected Z_{DR} using the (b) DP, (c) ZPHI, and (d) SCSC methods on data from 0055:37 UTC on 30 May 2004.

Fig. 7. Hydrometeor classification of (a) KOUN 0.0° data valid 0055 UTC and (b) UMass X-Pol 5.1° data corrected by the SCWC method valid 0055:37 UTC on 30 May 2009. The black lines in (a) represent the approximate sector scanned by UMass X-Pol and sampled in (b). Axes labels are relative to UMass X-Pol.

Fig. 8. A comparison of $Z_H^{'}$ from (a) 0.5° KVNX at 0059:33 UTC and (b) 2.46° UMass X-Pol at 0101:23 UTC on 13 May 2004. Processed ϕ_{DP} data and attenuation-correction Z_H using the ZPHI are contained in (c) and (d), respectively. Axes labels are relative to UMass X-Pol. The black ellipse in panel c highlights the area in which ϕ_{DP} decreases with range.

Fig. 9. UMass X-Pol (a) Z_{DR} (from the ZPHI method), (b) ρ_{HV}, (c) V_R, (d) hydrometeor classification (HC) valid 0101:53 UTC on 13 May 2004 at an elevation angle of 2.46°. The tornadic circulation is evident in all panels approximately 4 km due west of the radar location.

Fig. 10. UMass X-Pol data valid 0121:44 UTC on 13 May 2004 at 2.99°: (a) $Z_H^{'}$, (b) $Z_{DR}^{'}$, (c)

ρ_{HV}, (d) V_R, and (e) hydrometeor classification (HC). The black arrows in (b) mark the location of the Z_{DR} arc.

Fig. 11. A photograph of the shelf cloud associated with the QLCS on 21 May 2007 at 2350 UTC. The view is to the north from the same location as the mobile radar deployment. (Photograph courtesy of J. Snyder)

Fig. 12. Comparison of $Z_H^{'}$ from the (a) KAMA WSR-88D and (b) UMass X-Pol at 2339:50 UTC and 2338:51 UTC, respectively, on 21 May 2007. The elevation angle for KAMA is 0.52° and for the UMass X-Pol is 2.58°. Axis labels are relative to the location of the UMass X-Pol.

Fig. 13. UMass X-Pol (a) ϕ_{DP}, (b) $Z_H^{'}$, (c) Z_H (from ZPHI), (d) $Z_{DR}^{'}$, and (e) Z_{DR} (from DP) at 2.58° from 2338:51 UTC on 21 May 2007. Axis labels are relative to the location of the UMass X-Pol.

Fig. 14. (a) K_{DP} and (b) hydrometeor classification results using the ZPHI method from 2338:51 UTC on 21 May 2007 at an elevation angle of 2.58°.

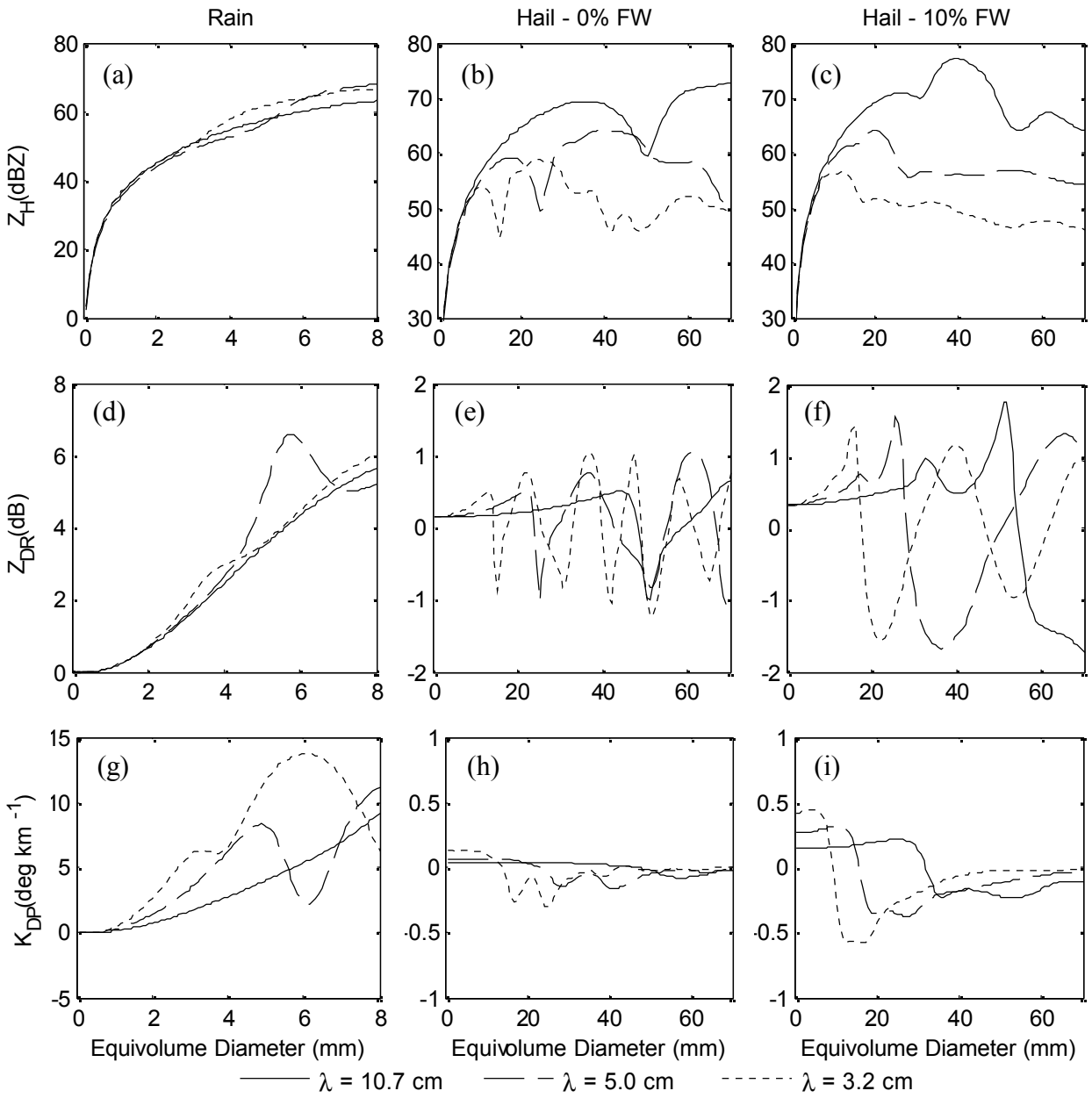

Fig. 1. A comparison of equivalent Z_H in (a) rain, (b) hail with 0% fractional water (FW; "dry hail"), and (c) hail with 10% fractional water content ("wet hail"); Z_{DR} in (d) rain, (e) dry hail, and (f) wet hail; K_{DP} in (g) rain, (h) dry hail, and (i) wet hail as a function of particle diameter in a monodispersed DSD. The solid, long dashed, and short dashed curves represent the solutions for 10.7 cm, 5 cm, and 3.2 cm wavelength radars, respectively, as a function of equivolume diameter. The values for rain were calculated for 10°C, mean canting angle and canting angle standard deviation of 0°, and with liquid water content of 10 g m^{-3}. The values for dry hail (i.e. no fractional water content) were calculated using ice content of 2 g m^{-3}, 0° mean canting angle, and 60° canting angle standard deviation [calculated from Jung et al. (2008)]. The values for the wet hail are the same as for the dry hail, except with a 55.2° canting angle standard deviation. The drop size-shape relation for rain is the same as described by Brandes et al. (2002).

Fig. 2. Photograph of the UMass X-Pol in the spring of 2007. (Photograph courtesy of J. Snyder)

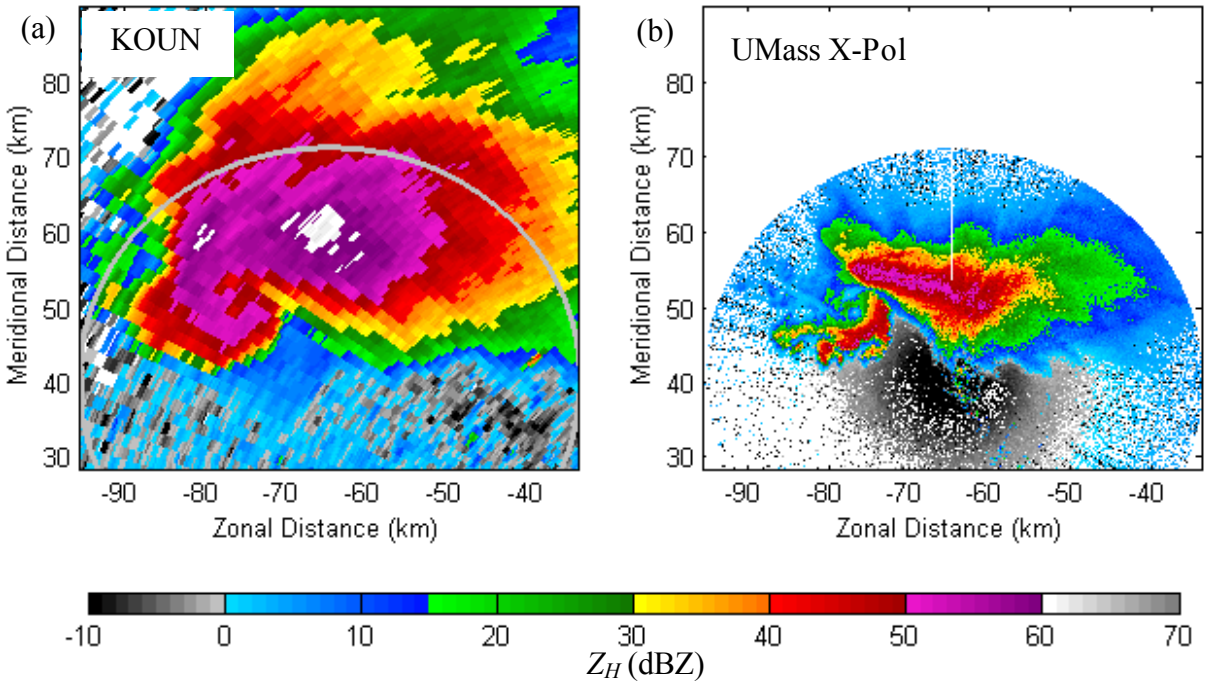

Fig. 3. A comparison of (a) 0.0° elevation angle data from KOUN and (b) 5.1° elevation angle data from UMass X-Pol valid 0044 UTC on 30 May 2004. Axes labels are relative to KOUN.

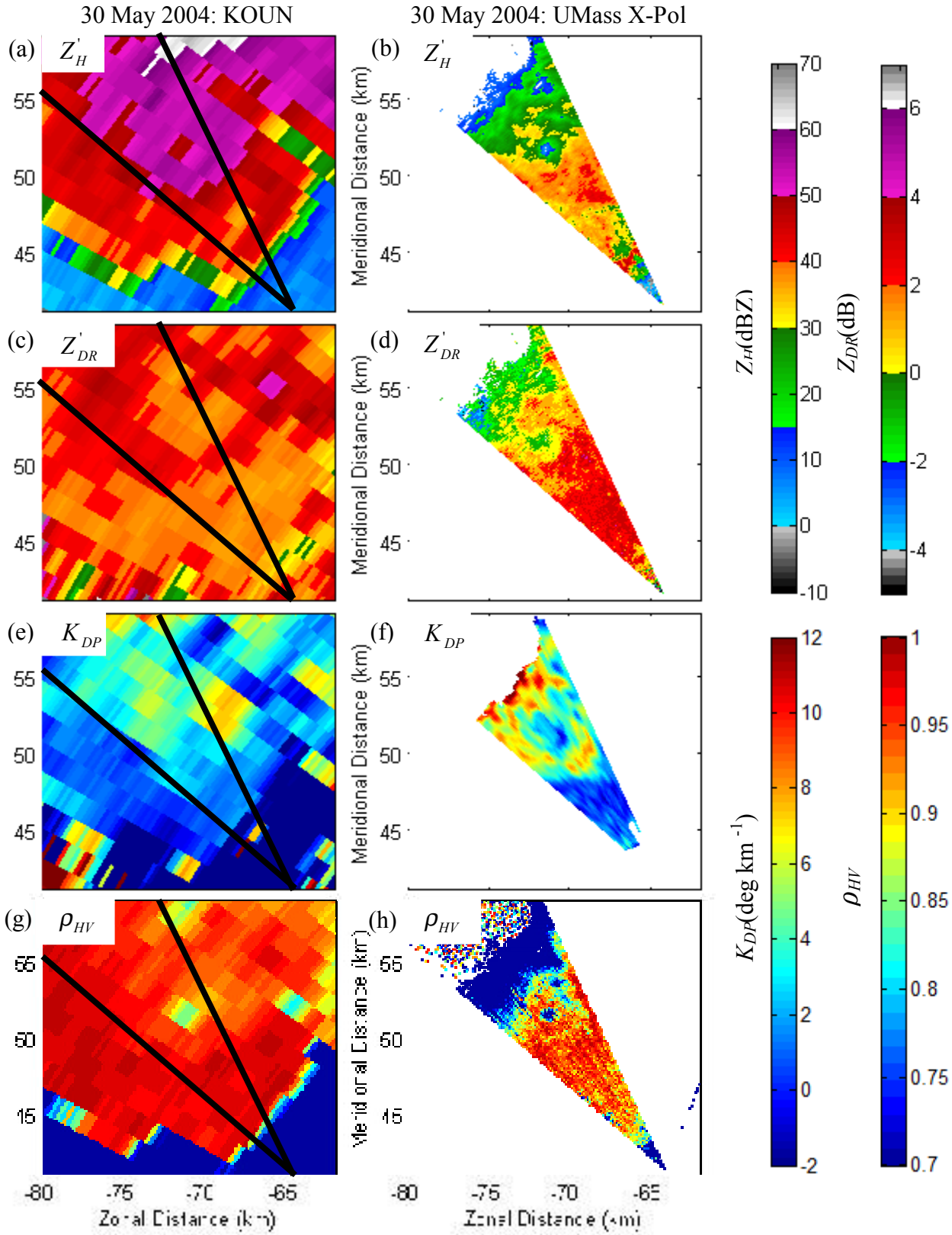

Fig. 4. Z_H' (a-b), Z_{DR}' (c-d), 3×K_{DP} and K_{DP} (e-f), and ρ_{HV} (g-h) from KOUN (0.0°) and UMass X-Pol (5.1°), respectively, at approximately 0055 UTC on the evening of 29 May 2004. Note

that K_{DP} for KOUN (e) has been scaled upward by a factor of 3. Axes labels relative to KOUN, and the black lines denote the approximate sector scanned by the UMass X-Pol.

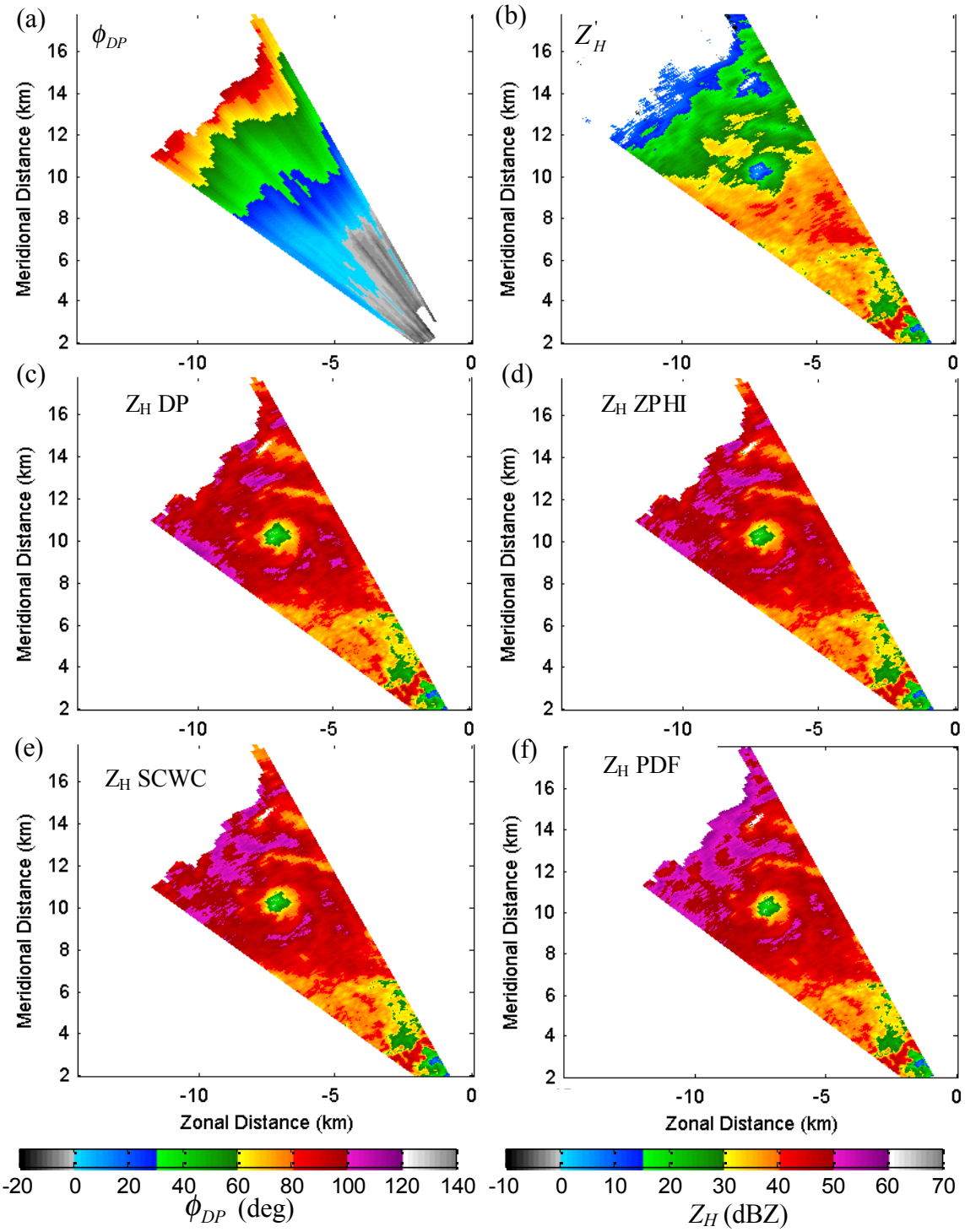

Fig. 5. UMass X-Pol (a) ϕ_{DP}, (b) $Z_H^{'}$, and attenuation-corrected Z_H using the (c) DP, (d) ZPHI, (e) SCWC, and (f) PDF techniques from 0055:37 UTC on 30 May 2004 at an elevation angle of 5.1°.

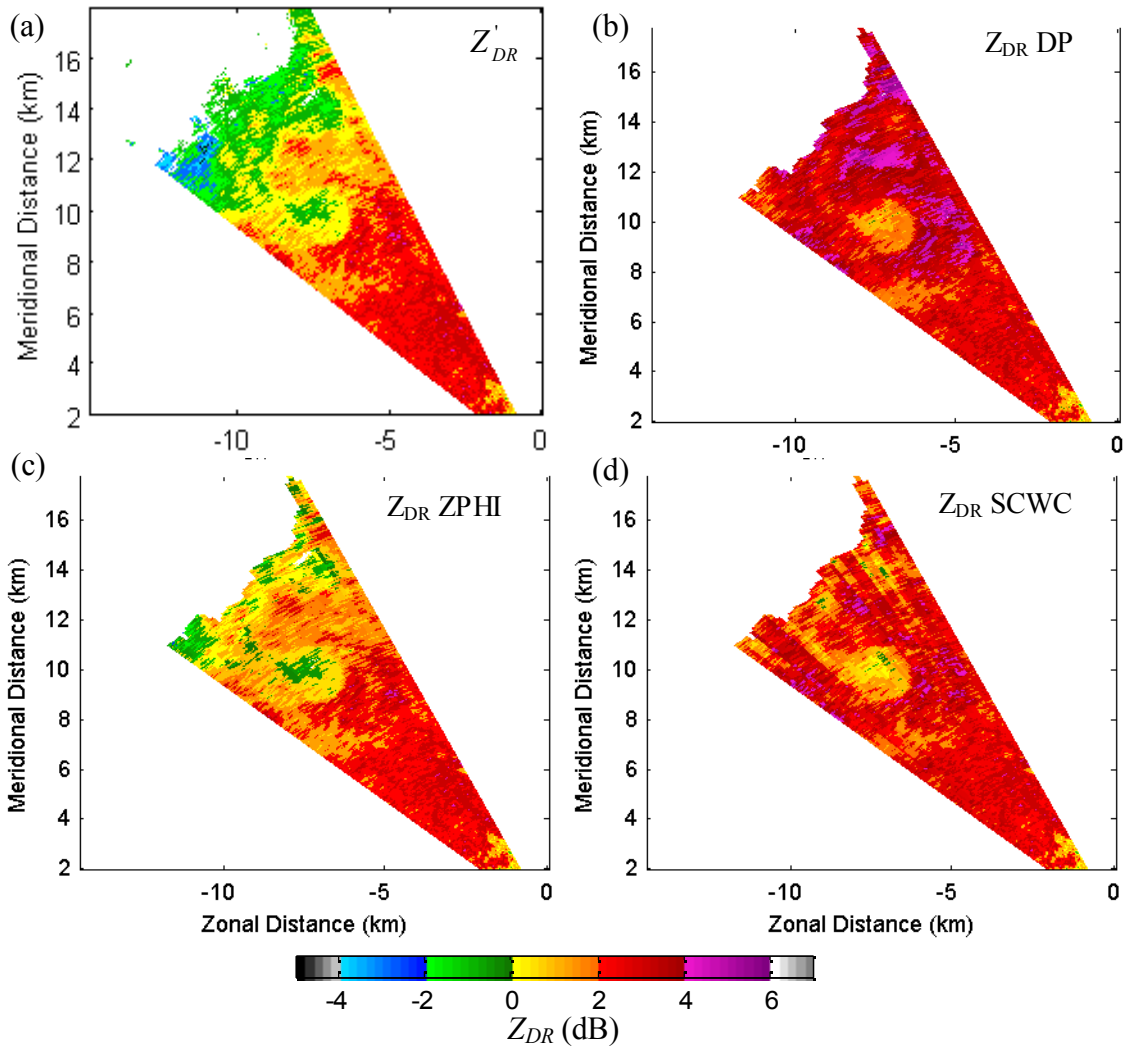

Fig. 6. UMass X-Pol (a) Z'_{DR} and attenuation-corrected Z_{DR} using the (b) DP, (c) ZPHI, and (d) SCSC methods on data from 0055:37 UTC on 30 May 2004.

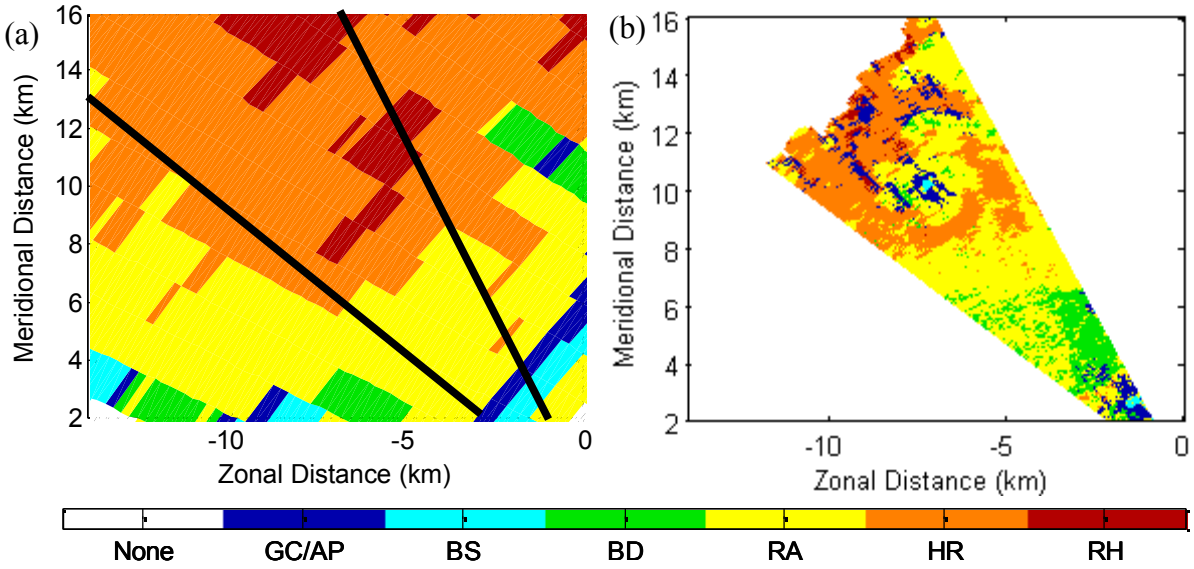

Fig. 7. Hydrometeor classification of (a) KOUN 0.0° data valid 0055 UTC and (b) UMass X-Pol 5.1° data corrected by the SCWC method valid 0055:37 UTC on 30 May 2009. The black lines in (a) represent the approximate sector scanned by UMass X-Pol and sampled in (b). Axes labels are relative to UMass X-Pol.

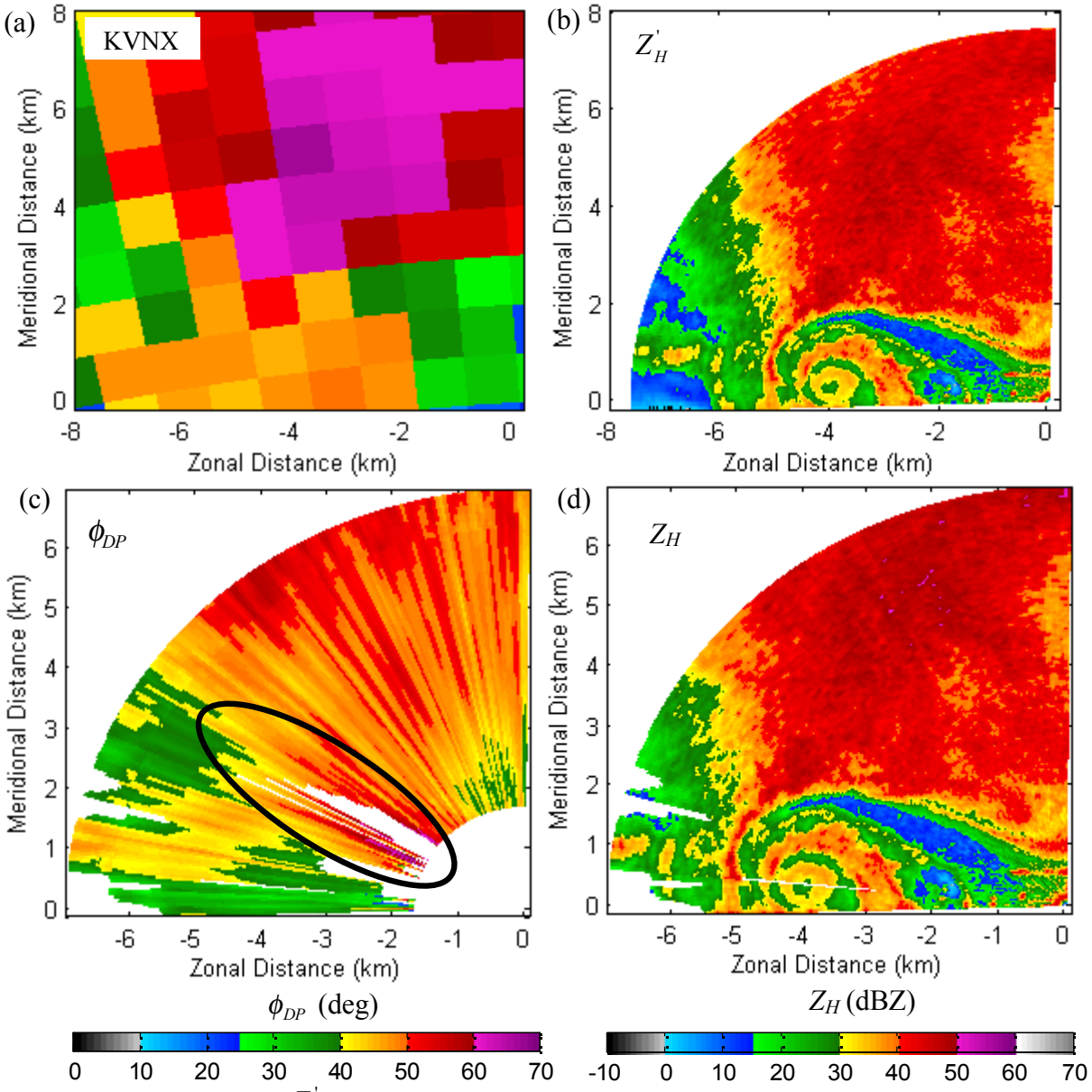

Fig. 8. A comparison of $Z_H^{'}$ from (a) 0.5° KVNX at 0059:33 UTC and (b) 2.46° UMass X-Pol at 0101:23 UTC on 13 May 2004. Processed ϕ_{DP} data and attenuation-correction Z_H using the ZPHI are contained in (c) and (d), respectively. Axes labels are relative to UMass X-Pol. The black ellipse in panel c highlights the area in which ϕ_{DP} decreases with range.

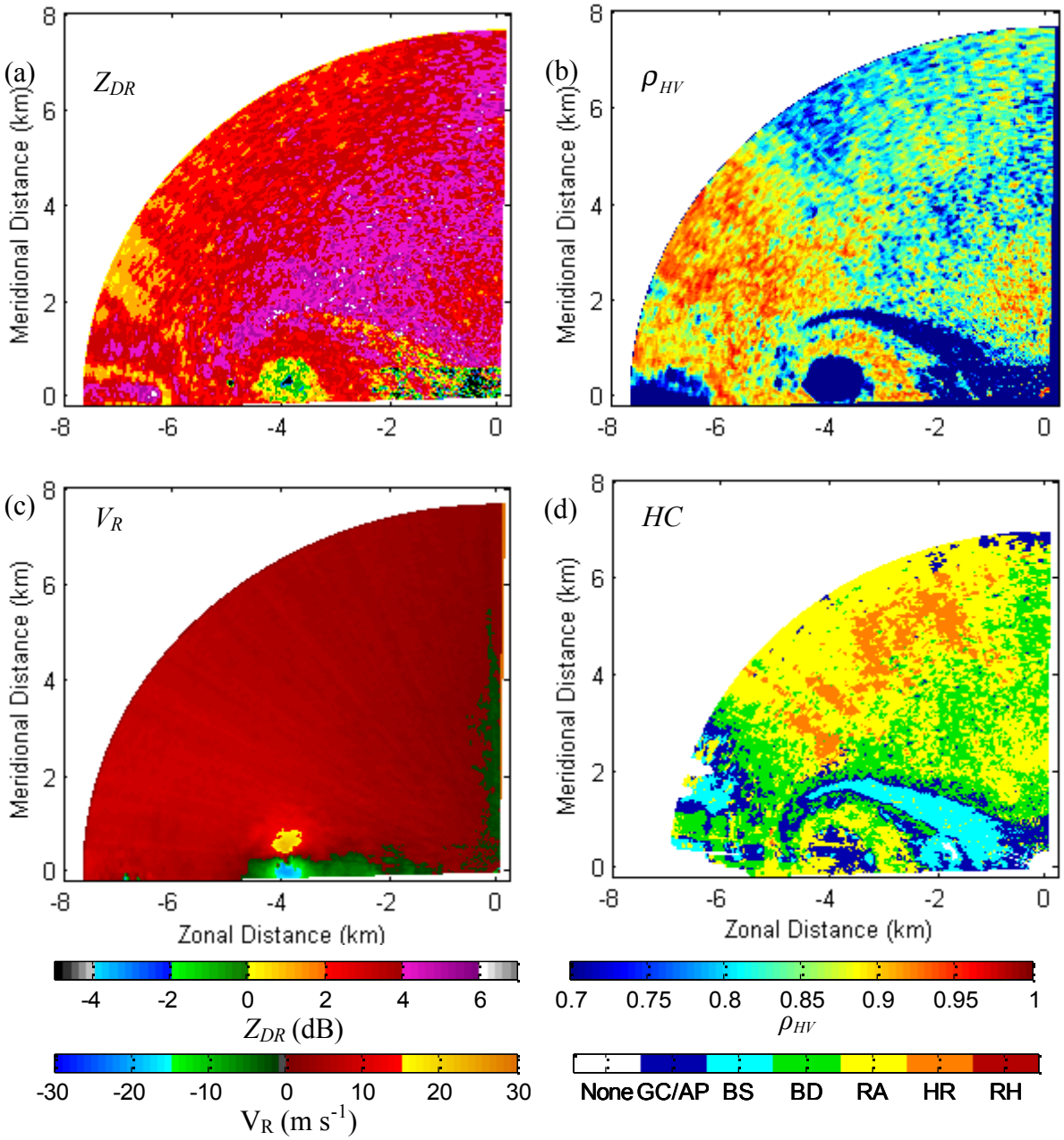

Fig. 9. UMass X-Pol (a) Z_{DR} (from the ZPHI method), (b) ρ_{HV} , (c) V_R, (d) hydrometeor classification (HC) valid 0101:53 UTC on 13 May 2004 at an elevation angle of 2.46°. The tornadic circulation is evident in all panels approximately 4 km due west of the radar location.

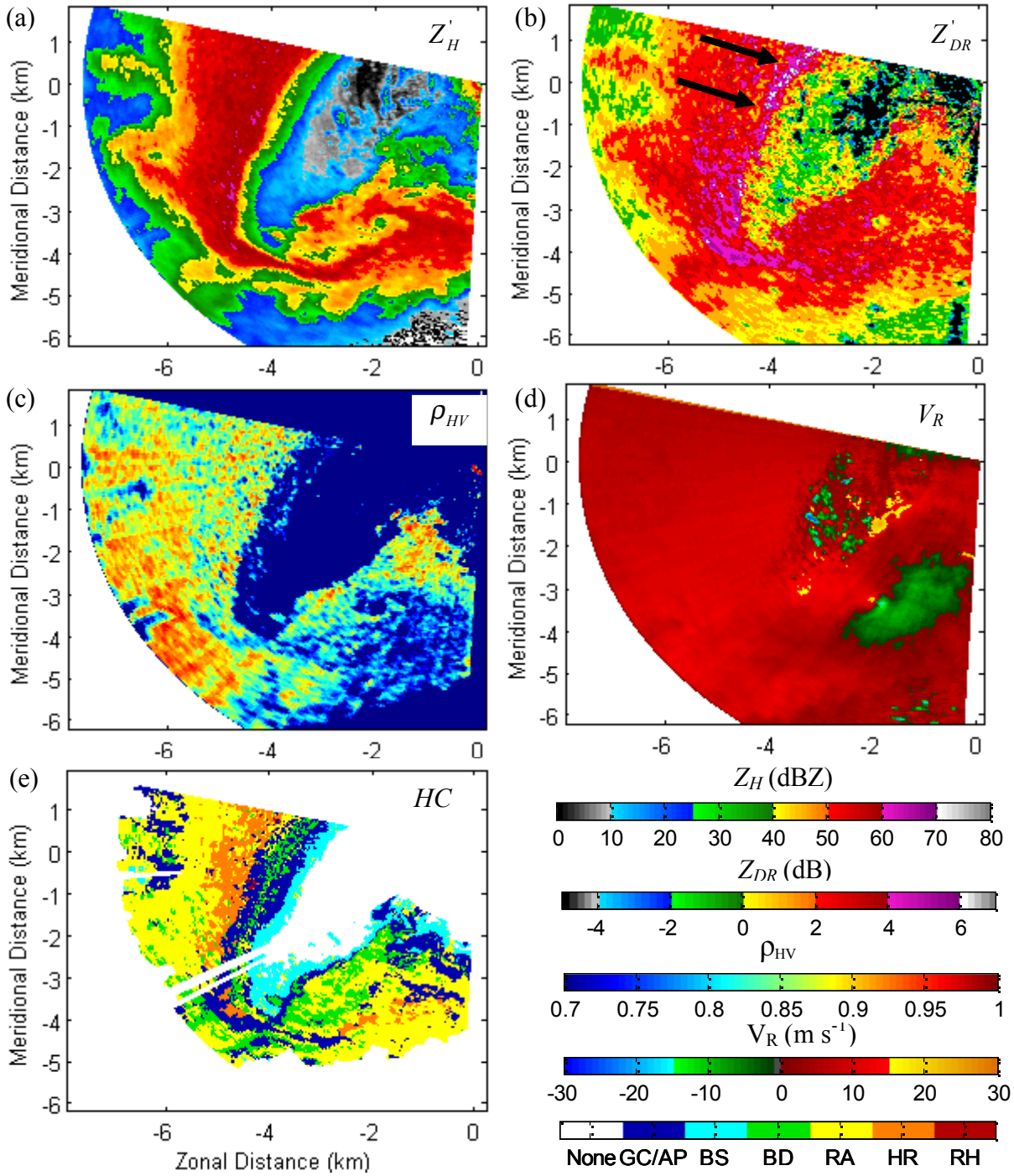

Fig. 10. UMass X-Pol data valid 0121:44 UTC on 13 May 2004 at 2.99°: (a) Z'_H, (b) Z'_{DR}, (c) ρ_{HV}, (d) V_R, and (e) hydrometeor classification (HC). The black arrows in (b) mark the location of the Z_{DR} arc.

Fig. 11. A photograph of the shelf cloud associated with the QLCS on 21 May 2007 at 2350 UTC. The view is to the north from the same location as the mobile radar deployment. (Photograph courtesy of J. Snyder)

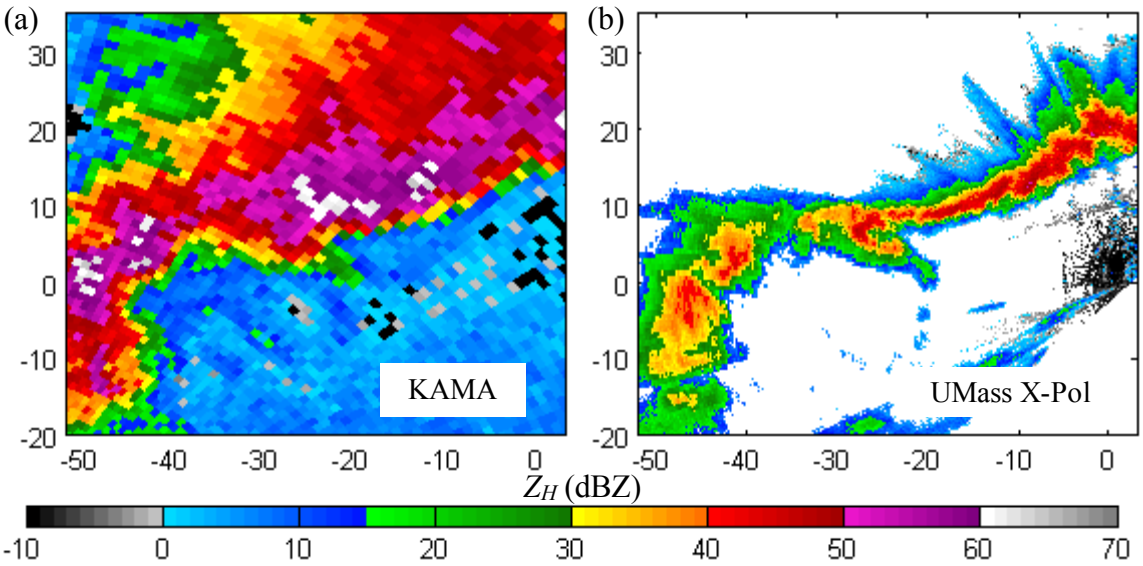

Fig. 12. Comparison of Z_H' from the (a) KAMA WSR-88D and (b) UMass X-Pol at 2339:50 UTC and 2338:51 UTC, respectively, on 21 May 2007. The elevation angle for KAMA is 0.52° and for the UMass X-Pol is 2.58°. Axis labels are relative to the location of the UMass X-Pol.

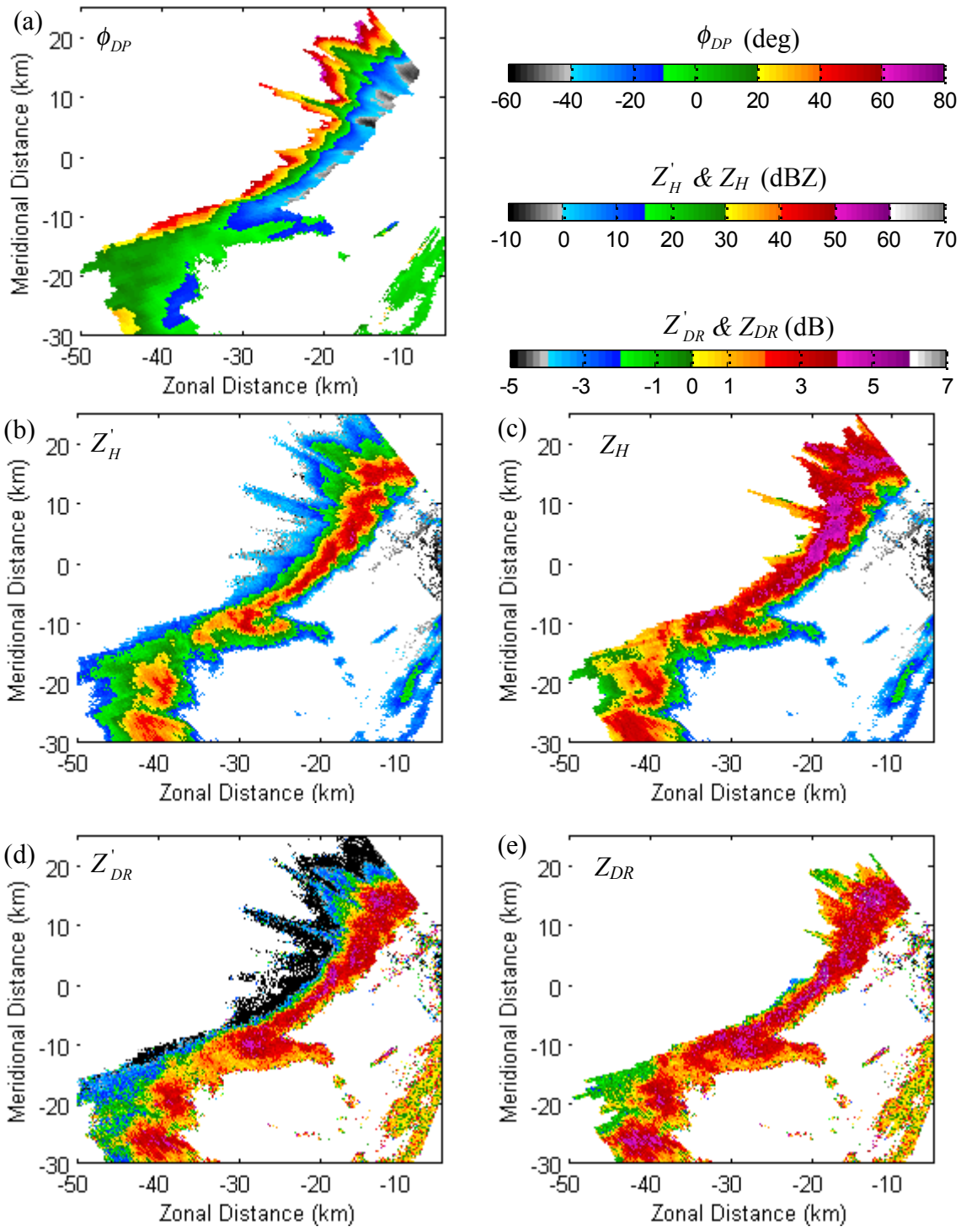

Fig. 13. UMass X-Pol (a) ϕ_{DP}, (b) $Z_H^{'}$, (c) Z_H (from ZPHI), (d) $Z_{DR}^{'}$, and (e) Z_{DR} (from DP) at 2.58° from 2338:51 UTC on 21 May 2007. Axis labels are relative to the location of the UMass X-Pol.

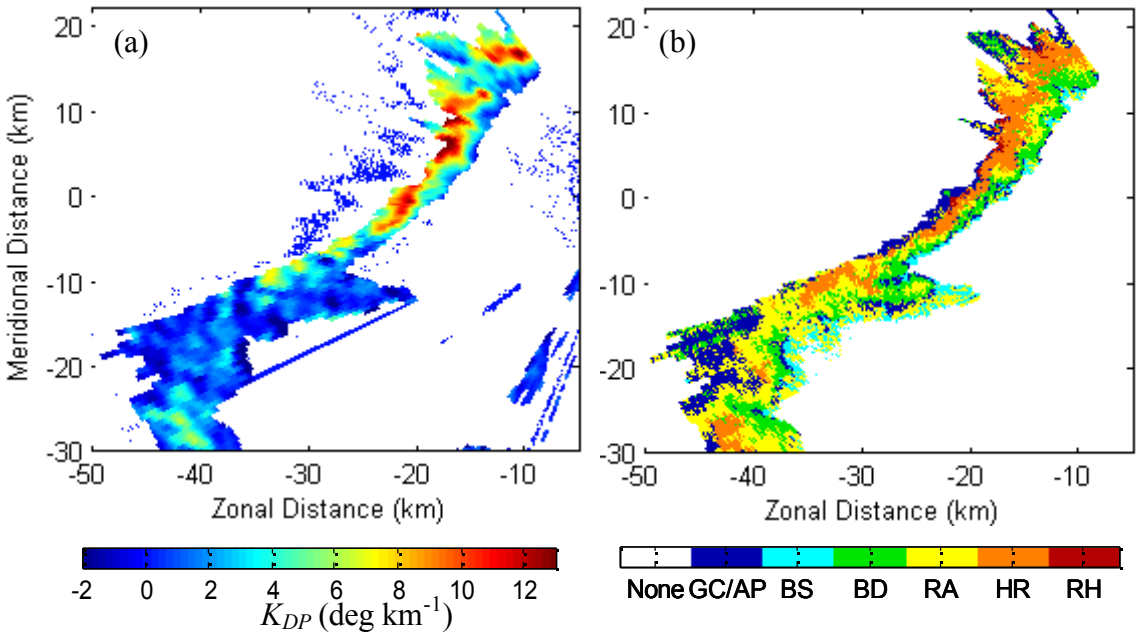

Fig. 14. (a) K_{DP} and (b) hydrometeor classification results using the ZPHI method from 2338:51 UTC on 21 May 2007 at an elevation angle of 2.58°.

TABLE 1. An overview of the main attenuation correction schemes used in this paper; the short-hand abbreviations, references, and required a priori constants (with reference to the associated equations) for each technique are shown.

Method	Reference(s)	Required Constants
$A_{H,DP}$-K_{DP} Parameterization (DP)	Bringi et al. (1990)	(5) $b = 0.76$ (6) $\alpha_H = 0.313$ (7) $\alpha_{DP} = 0.0483$
ZPHI Rain-Profiling (ZPHI)	Testud et al. (2000)	
Self-Consistent with Constraints (SCWC)	Bringi et al. (2001); Park et al. (2005b)	
Pseudo-Dual-Frequency (PDF)	Zhang et al. (2004)	

TABLE 2. The output classifiers used in this study.

ID #	Abbrev.	Description
1	CG/AP	Ground clutter / anom. propagation
2	BS	Biological scatterers
3	BD	Big drops
4	RA	Light to moderate rain
5	HR	Heavy rain
6	RH	Rain - hail mixture

TABLE 3. Hydrometeor classification membership function parameters used for the X-band data in this study. Some membership functions for Z_{DR} and LK_{DP} are two-dimensional functions of Z_H: $A1 = 3.2\times10^{-5} Z_H^{\ 3} - 0.0017 Z_H^{\ 2} + 0.042 Z_H - 0.39$,

$A2 = -4.1\times10^{-5} Z_H^{\ 3} + 0.0059 Z_H^{\ 2} - 0.096 Z_H + 0.49$, $A3 = 4.85\times10^{-4} Z_H^{\ 2} + 6.67\times10^{-2} Z_H + 1.42$,

$B1 = 0.7 Z_H - 42$, and $B2 = 0.7 Z_H - 28$.

		X1	X2	X3	X4
Z_H	GC/AP	15	20	70	80
	BS	5	10	20	30
	BD	24	29	49	54
	RA	5	10	45	50
	HR	42	47	57	62
	RH	40	45	65	70
Z_{DR}	GC/AP	-4	-2	1	2
	BS	0	2	10	12
	BD	A2-0.6	A2-0.3	A3	A2+1
	RA	A1-0.3	A1	A2	A2+0.5
	HR	A1-0.3	A1	A2	A2+0.5
	RH	-0.3	0	A1	A1+0.5
LK_{DP}	GC/AP	-30	-25	10	20
	BS	-30	-25	10	11
	BD	B1-1	B1	B2-3	B2-1
	RA	B1-1	B1	B2	B2+1
	HR	B1-1	B1	B2	B2+1
	RH	-10	-4	B1	B1+1
ρ_{HV}	GC/AP	0.5	0.6	0.9	0.95
	BS	0.3	0.5	0.8	0.83
	BD	0.92	0.93	1.00	1.01
	RA	0.95	0.96	1.00	1.01
	HR	0.92	0.94	1.00	1.01
	RH	0.80	0.85	0.95	1.01
$SD(Z_H)$	GC/AP	2	6	15	20
	BS	1	2	4	7
	BD	0	0.5	5	8
	RA	0	0.5	5	8
	HR	0	0.5	5	8
	RH	0	0.5	5	8
(Φ	GC/AP	20	30	50	60
	BS	8	10	40	60

	BD	0	1	15	30
	RA	0	1	15	30
	HR	0	1	15	30
	RH	0	1	15	30

TABLE 4. Characteristics of the UMass X-Pol as it was configured in and prior to 2007.

Physical characteristics	
Operating Frequency	9.41 GHz
Antenna Diameter	1.8 m
Antenna 3 dB Beamwidth	1.25°
Transmission characteristics	
Peak Power (H+V)	25 kW
Pulse Length	1 μs
Range Resolution	150 m
PRF	1.6 kHz & 2.0 kHz
Receiving characteristics	
Sampling Resolution	Pre-2007: 15 m; 2007: 60 m
Receiver Dynamic Range	~73 dB
Receiver Gain	~45 dB

TABLE 5. MAE, bias, and bias-corrected MAE (in dB) of correction techniques at different upper reflectivity thresholds and κ (Barnes analysis smoothing parameter) values calculated from the 0055:37 UTC scan on 30 May 2004. "Threshold" is the upper-bound for Z_H^S used in the calculations (i.e. only bins with Z_H^S lower than the threshold are compared) and is given in dBZ.

κ	1	1	1	4	8
Threshold	55	None	50	55	55
			MAE		
DP	7.1	7.2	6.2	7.2	7.3
ZPHI	6.7	6.8	5.9	6.7	6.8
SCWC	6.6	6.7	5.9	6.7	6.7
			BIAS		
DP	-6.1	-6.2	-4.3	-6.6	-6.7
ZPHI	-5.6	-5.8	-4.0	-6.1	-6.2
SCWC	-5.5	-5.7	-4.0	-6.0	-6.1
			BCMAE		
DP	4.3	4.3	4.5	3.9	3.9
ZPHI	4.2	4.2	4.5	3.8	3.7
SCWC	4.2	4.2	4.5	3.8	3.7